NASA TECHNICAL NOTE

NASA TN D-4800

NASA TN D-4800

EXPERIMENTAL BASE PRESSURES ON 9° SPHERICALLY BLUNTED CONES AT MACH NUMBERS FROM 10.5 TO 20

by Charles G. Miller III

Langley Research Center
Langley Station, Hampton, Va.

NATIONAL AERONAUTICS AND SPACE ADMINISTRATION • WASHINGTON, D. C. • OCTOBER 1968

EXPERIMENTAL BASE PRESSURES ON 9° SPHERICALLY BLUNTED CONES AT MACH NUMBERS FROM 10.5 TO 20

By Charles G. Miller III

Langley Research Center
Langley Station, Hampton, Va.

NATIONAL AERONAUTICS AND SPACE ADMINISTRATION

For sale by the Clearinghouse for Federal Scientific and Technical Information
Springfield, Virginia 22151 – CFSTI price $3.00

EXPERIMENTAL BASE PRESSURES ON 9° SPHERICALLY BLUNTED CONES AT MACH NUMBERS FROM 10.5 TO 20

By Charles G. Miller III
Langley Research Center

SUMMARY

Base pressure measurements were obtained in the Langley hotshot tunnel at an angle of attack of 0° for a series of cones having semiapex angles of 9° and bluntness ratios of 0, 0.3, 0.55, and 0.8. Nominal free-stream Mach numbers were 10.6, 13.8, 15.6, and 19.6 and free-stream Reynolds numbers, based on model surface length, were approximately 0.02×10^6 to 2×10^6 in nitrogen. These conditions were assumed to result in laminar boundary-layer flow. Sting surface pressure distributions and sting tuft flow patterns were obtained 0 to 3.75 model base diameters downstream of the model base.

Base pressure measurements obtained 0.21 to 0.83 base radius from the model axis showed the existence of radial base pressure gradients for all bluntness ratios over the entire Mach number and Reynolds number range, with the base pressure increasing toward the model axis. The existence of a radial base pressure gradient is in agreement with several other investigations having laminar boundary-layer and near-wake flow but in opposition to those having transitional or turbulent boundary-layer and near-wake flow. The ratio of area-mean base pressure to stagnation pressure behind a normal shock for the spherically blunted cones was relatively insensitive to Reynolds number for Reynolds numbers greater than 0.1×10^6 but decreased with decreasing Reynolds number for Reynolds numbers less than 0.1×10^6 for all bluntness ratios. This area-mean base pressure ratio increased with decreasing Mach number and increasing bluntness ratio. A semiempirical method for estimating the laminar base pressure ratio of spherically blunted cones in hypersonic flow for Reynolds numbers, based on model surface length, from 0.1×10^6 to 1×10^6 was found to yield reasonable agreement with the present measured base pressure results. The contribution of base drag to total inviscid drag decreased with increasing bluntness ratio and increasing Mach number. The base drag was less than approximately 2 percent of the total inviscid drag for bluntness ratios of 0.55 and 0.8 over the entire Mach number range but was approximately 15 percent for the pointed cone and approximately 5 percent for the bluntness ratio of 0.3 at a Mach number of 10.6.

INTRODUCTION

The base drag of reentry vehicles is of considerable practical importance since, in some instances, base drag can account for an appreciable portion of the total drag. Related to the base-drag problem is the problem of determining near-wake flow-field characteristics which are of current interest due, in part, to their role in discrimination of reentry configurations. A parameter essential to the study of base drag or analysis of the flow in the near-wake region is base pressure. Although numerous base pressure investigations have been performed at supersonic and low hypersonic Mach numbers (see, for example, refs. 1 to 8), only a few investigations (refs. 8 to 12) have been made at Mach numbers in excess of 10.

To help alleviate this scarcity of hypersonic base pressure data, a systematic investigation was conducted in the Langley hotshot tunnel to determine the effect of Mach number, Reynolds number, and bluntness ratio on base pressure. A family of spherically blunted cones having semiapex angles of 9° and bluntness ratios of 0, 0.3, 0.55, and 0.8 were tested at an angle of attack of 0° for nominal free-stream Mach numbers of 10.6, 13.8, 15.6, and 19.6 and for free-stream Reynolds numbers, based on model surface length, of approximately 0.02×10^6 to 2×10^6 in nitrogen. The present study included radial base pressure distributions, sting axial-pressure distributions, and sting tuft flow patterns. Results from this experimental investigation are presented along with laminar theoretical and turbulent semiempirical predictions.

SYMBOLS

The units used for the physical quantities in this paper are given both in the U.S. Customary Units and in the International System of Units (SI). Conversion factors relating the two systems are given in reference 13.

C_D drag coefficient

d diameter

D sting diameter

l sting length

M Mach number

p	pressure
$\bar{p}_b$	area-mean base pressure (eq. (2))
q	dynamic pressure
r	radius
R	Reynolds number
s	model surface length, measured from model stagnation point at $\alpha = 0^o$ (fig. 3)
T	temperature
x	distance along sting from model base
α	angle of attack
β	dividing-streamline turning angle (fig. 16)
λ	mean free path
μ	coefficient of viscosity
ψ	bluntness ratio, r_n/r_b
θ	model semiapex angle

Subscripts:

b	model base
L	local conditions immediately ahead of model base
n	model nose

r	base recirculation region
s	based on model surface length
t,1	arc-chamber conditions following arc discharge
t,2	stagnation conditions behind normal shock
w	wall
x	distance along sting from model base
y	distance across model base, measured from model axis
∞	free-stream conditions

Superscript:

*	conditions at nozzle throat

FACILITY AND APPARATUS

Facility and Tests

The Langley hotshot tunnel is a hypervelocity, arc-heated, blowdown wind tunnel. The major components of this facility include a capacitor bank and electrical collector, an arc chamber, a 10° total-divergence-angle conical nozzle and test section, a 10° cone-cylinder diffuser, and a vacuum reservoir. A more detailed description of this facility is presented in reference 14.

In the present study, free-stream Mach numbers of approximately 10.6, 13.8, 15.6, and 19.6 were obtained in nitrogen by employing several nozzle throat diameters and several arc-chamber stagnation temperatures for an arc-chamber stagnation pressure within ±10 percent of 8200 psia $\left(56.5\ MN/m^2\right)$. The free-stream Mach numbers, corresponding unit free-stream Reynolds numbers, nozzle throat diameters, and nominal arc-chamber stagnation pressure and temperatures for the present investigation are given in the following table:

M_∞	R_∞		d^*		$p_{t,1}$		$T_{t,1}$	
	per ft	per meter	in.	mm	psia	MN/m^2	^oR	^oK
10.6	0.74×10^6	2.43×10^6	0.500	12.70	8200	56.5	6300	3500
13.8	.33	1.08	.250	6.35	8200	56.5	6300	3500
	.47	1.54	.250	6.35	8200	56.5	5400	3000
	2.20	7.20	.375	9.52	8200	56.5	2800	1550
15.6	.14	.46	.150	3.81	8200	56.5	8100	4500
19.6	.07	.23	.075	1.91	8200	56.5	7900	4400
	.14	.46	.100	2.54	8200	56.5	6300	3500
	.85	2.79	.150	3.81	8200	56.5	2900	1600

The tunnel test time varied from 0.03 to 0.12 sec, depending on the nozzle throat diameter employed. Calibration results in nitrogen for the preceding nozzle throat diameters are presented in reference 14. These results imply that a maximum nozzle axial Mach number gradient of 0.056 per in. (2.2 per m) was experienced in the present study.

Models and Model Support System

The models were 9° semiapex angle, spherically blunted cones having bluntness ratios r_n/r_b ranging from 0 for the pointed cone to 0.8 for the bluntest configuration. Interchangeable forebodies, shown in figure 1, were fabricated from aluminum and matched to a stainless-steel cone-frustum afterbody having a 3.00-in. (7.62-cm) base diameter. A sketch of the models is presented in figure 2. The model support arrangement, model bases, and instrumentation locations are illustrated in figure 3. As shown in figure 3(a), a single pressure orifice was located on the model surface immediately upstream (0.042 base diameter) of the base plane of the models having $D/d_b = 0.583$. For the base pressure measurements, model base A, shown in figure 3(b), was used in conjunction with cylindrical sting A (fig. 3(a)), having $D/d_b = 0.125$ and $l/d_b = 6$, and had 4 pressure orifices positioned at 0.208-base-radius increments from the model axis. Sting B, having $D/d_b = 0.583$ and $l/d_b = 12$, was fabricated with 15 pressure orifices located as shown in figure 3(a). Model base B was used in conjunction with sting B and was instrumented with six equally spaced orifices located on a circle with a radius of 0.833 base radius. All pressure orifices were 0.067 in. (1.7 mm) in diameter.

The model base plane was located at a constant nozzle axial station of 124.5 in. (3.16 m) (see ref. 14 for relative nozzle-axial-station locations) to maintain a constant

ratio of sting length to base diameter for each sting for a given strut location. Thus, as the model bluntness ratio increased from 0 to 0.8, the model nose moved downstream 6.5 in. (16.5 cm).

Instrumentation

Variable-reluctance pressure transducers (ref. 15) were employed in the present investigation for all model and pitot pressure measurements. Geometric details of the barrel-type pressure transducers used to measure base pressures, sting pressures, and afterbody pressures less than 0.1 psia $\left(690\ N/m^2\right)$ are shown in figure 4(a). (Fig. 4 is taken directly from ref. 11.) The wafer-type pressure transducers employed to measure afterbody pressures greater than 0.1 psia and test-section pitot pressure are described in reference 15. The reference side of all model and sting pressure transducers was maintained at a constant pressure of approximately 0.00004 psia $\left(0.28\ N/m^2\right)$ by an external vacuum source for all calibrations and tests. These pressure transducers were calibrated under vacuum for the pressure range anticipated for each tunnel test. A high-precision capacitive pressure meter was employed as a calibration standard for the transducers calibrated under vacuum. A typical calibration curve for the barrel-type pressure transducer is shown in figure 4(b). The wafer-type pressure transducers were calibrated by utilizing a bellows and manometer system. Arc-chamber stagnation pressure was measured by a high-response strain-gage transducer having a full-scale rating of 20 000 psia $\left(138\ MN/m^2\right)$. All pressure transducers were excited by 5-volt 20-kilocycle carrier amplifiers. The output signals from the amplifiers drove galvanometers in an oscillograph. A typical oscillograph record illustrating base, afterbody, pitot, and arc-chamber pressure traces obtained at a Mach number of 20 are shown in figure 7 of reference 11.

In order to estimate the dividing-streamline turning angle of the base flow, strands of cotton thread 0.25 in. (6.35 mm) in length were positioned along the sting having $D/d_b = 0.583$ as shown in figure 5(a). Movement of the tufts during a tunnel run was determined from schlieren photographs (see fig. 5(b), for example).

Accuracy

Uncertainties involved in the pressure measurements are based on instrumentation calibration linearity, repeatability, and zero shift and on quality of oscillograph traces with respect to the signal-to-noise ratio and pressure decay with tunnel run time. For the most unfavorable conditions, the test-section pitot pressure measurements were believed to have a maximum probable inaccuracy of approximately ±5 percent, the arc-chamber stagnation pressure measurements were believed accurate to within ±10 percent, and the model surface pressure measurements immediately ahead of the base were

believed accurate to approximately ±15 percent. Base and sting pressure measurements corresponding to pressures greater than 0.004 psia $\left(27.6\ N/m^2\right)$ were believed to have a maximum probable inaccuracy of approximately ±20 percent whereas pressures less than 0.004 psia were believed to have a maximum probable inaccuracy of approximately ±30 percent.

Data Reduction and Correction For Orifice Effect

The initial arc-chamber density was determined from the initial arc-chamber pressure and ambient temperature. This initial density and the measured values of arc-chamber stagnation pressure and test-section pitot pressure were the basic input data for the real-nitrogen data-reduction program presented in reference 16. Free-stream conditions for all tunnel tests were computed from pitot pressure measurements made at the nozzle axial stations corresponding to the model noses. The theoretical results of reference 17 indicate the possible existence of vibrational-nonequilibrium flow for the present arc-chamber stagnation conditions and nozzle geometry. However, as discussed in the appendix of reference 14, the experimental results of reference 18 showed that vibrational relaxation rates are faster than existing theoretical predictions. Because of this existing uncertainty associated with vibrational relaxation rates, no corrections for the effects of vibrational nonequilibrium were applied to the present calculated free-stream flow parameters.

Since base pressures as low as 0.0002 psia $\left(1.4\ N/m^2\right)$ were measured in the present investigation, the effects of response time, orifice diameter, and other phenomena described in reference 19 were considered on the measured base pressures. For the present orifice diameter of 0.067 in. (1.7 mm) and tubing lengths from 0.5 to 0.75 in. (12.7 to 19 mm), it can be inferred from reference 20 that pressure lag times as high as 0.025 sec could exist for the lowest base pressure being measured. However, since the present base pressures at these low-pressure conditions were measured at tunnel elapsed run times between 0.05 and 0.09 sec and the oscillograph traces indicated no significant pressure lag, no pressure-lag correction was made to the data.

Consideration was then given to the need for an orifice-effect correction to the base pressure measurements as discussed in reference 19. By assuming ideal-gas behavior in the base recirculation region and using the coefficient of viscosity relation of reference 16 for nitrogen, the relation of reference 19 for the mean free path in nitrogen was expressed as

$$\lambda_r = \left(0.1697 \times 10^{-6}\right)\frac{T_r^{\,2}}{p_b\left(T_r + 100\right)} \tag{1}$$

where λ_r was the mean free path in inches, p_b was the measured base pressure in psia, and T_r was the temperature in ^{o}K in the base recirculation region as obtained from the isentropic flow relations of reference 21 in conjunction with the measured base pressures and measured stagnation pressure behind a normal shock (pitot pressure). The mean free paths were found to be nearly equal to or greater than the orifice diameter for the Mach 19.6 tests at the lower free-stream Reynolds numbers; thus, the possible existence of free molecular flow is indicated. To determine the base heat-transfer rates necessary for application of the working chart of reference 19, the model base was instrumented with 4 calorimeter thermocouple gages having a 0.001-in.-thick (0.0025-cm) 302 stainless-steel skin with a chromel-alumel thermocouple welded to the inner surface. (A detailed description of this technique is presented in ref. 22.) The tests at Mach 19.6 illustrated that base heat-transfer rates could be obtained with only limited success at these conditions with the present measuring technique. This was due to the low level of base heat-transfer rates at Mach 19.6 (on the order of 0.05 to 0.2 Btu/ft^2-sec (5.7×10^2 to 22.7×10^2 W/m^2)) and the short run time of the tunnel (less than 0.12 sec). However, the results which were obtained for all bluntness ratios were observed to be in reasonable agreement with the free-flight base heat-transfer-rate correlation of reference 23. Therefore, the correlation of reference 23 was employed to estimate the present base heat-transfer rates. (The stagnation-point heat-transfer rate was calculated by use of the theory of Fay and Riddell (ref. 24).) The model surface temperature T_w was assumed to remain at 530^{o} R (294^{o} K) during the short run time of the tunnel. For the lowest measured base pressure at Mach 10.6, the maximum applied correction was less than 1 percent; at Mach 13.8, less than 10 percent; at Mach 15.6, less than 20 percent; and at Mach 19.6, less than 50 percent.

RESULTS AND DISCUSSION

To take advantage of the versatility of the Langley hotshot tunnel, this investigation was conducted for free-stream Mach numbers from approximately 10.6 to 19.6. Unfortunately, there was an accompanying variation in unit free-stream Reynolds number per ft from 0.74×10^6 to 0.14×10^6 (2.43×10^6 to 0.46×10^6 per m). In an attempt to separate the effects on base pressure of variation in Mach number from those of variation in Reynolds number, the investigation included tests for a range of unit free-stream Reynolds number per ft from 0.33×10^6 to 2.20×10^6 (1.08×10^6 to 7.20×10^6 per m) for a free-stream Mach number that was within ±3 percent of being constant at 13.8 and a range of unit Reynolds number per ft from 0.07×10^6 to 0.85×10^6 (0.23×10^6 to 2.79×10^6 per m) for a free-stream Mach number that was within ±5 percent of being constant at 19.6. Based on the results presented in reference 25, it is assumed that the present test conditions result in laminar boundary-layer flow and laminar near-wake flow.

Radial Base Pressure Distribution

Radial base pressure distributions for model bluntness ratios 0, 0.3, 0.55, and 0.8 are shown in figure 6 for the present Mach numbers and corresponding Reynolds numbers based on model surface length. The measured base pressures (fig. 6) are nondimensionalized by using the stagnation pressure behind a normal shock primarily because this pressure is a measured quantity in the present investigation and is essentially independent of the effects of possible vibrational-nonequilibrium flow. From figure 6, it may be observed that a pressure gradient across the base exists for all bluntness ratios and Mach numbers, with the base pressure increasing toward the model axis $\left(r_y/r_b = 0\right)$. The magnitude of the radial base pressure gradient $\left|\frac{\Delta\left(p_b/p_{t,2}\right)}{\Delta\left(r_y/r_b\right)}\right|$ is shown in figure 7 as a function of Reynolds number, based on model surface length, for the present range of Mach numbers and model bluntness ratios. The gradients of figure 7 were obtained by applying a linear curve fairing (when possible) to the data of figure 6; the uncertainty involved in determining the radial base pressure gradients is indicated by the barred lines through the symbols in figure 7. At Mach 13.8 (fig. 7(b)), an influence of Reynolds number on the radial base pressure gradient is observed for the pointed cone ($\psi = 0$); whereas, no significant influence of Reynolds number is observed on the radial base pressure gradient for the spherically blunted cones. At Mach 19.6 (fig. 7(d)), the radial base pressure gradient is observed to be dependent on Reynolds number for all bluntness ratios. In most instances, the radial base pressure gradient increases with increasing bluntness ratio for a constant Mach number and unit Reynolds number. Figure 8, which is a summary of the results of figure 7, shows that a Mach number dependence may exist with the radial base pressure gradient increasing somewhat as the Mach number increases from 10.6 to 13.8. Radial base pressure gradients, where the base pressure increases in the direction of the model axis $\left(r_y/r_b = 0\right)$, have also been observed in references 4 and 12 and seem to be characteristic of axisymmetric bodies having laminar boundary-layer and near-wake flow. Bodies having transitional or fully turbulent boundary layers or near wakes appear to have negligible variation in pressure across the base (refs. 1, 2, 3, and 8).

Area-Mean Base Pressure

To obtain representative values of base pressure, an area-mean determination of base pressure was made with the equation

$$\bar{p}_b = \frac{1}{\pi r_b^2}\int_0^{r_b} p_b\left(r_y\right) 2\pi r_y dr_y \tag{2}$$

where $p_b\left(r_y\right)$ is the base pressure at radius r_y. This equation states that the area-mean base pressure is represented by the area under the curve resulting from a plot of

p_b as a function of $(r_y/r_b)^2$. The accuracy of obtaining the area-mean base pressure from equation (2) is subject to question because of the uncertainty of the extrapolation of the base pressure distribution between values of r_y/r_b from 0 to 0.21 and from 0.83 to 1. However, it should be noted that relatively large errors in the extrapolation to $r_y/r_b = 0$ result in a small error in the area-mean base pressure since p_b is plotted as a function of $(r_y/r_b)^2$. The $(r_y/r_b)^2$ term could be more critical for the extrapolation between $r_y/r_b = 0.83$ and 1 except that the base pressure is usually small in this region; therefore, the errors contributed to the area-mean base pressure by this extrapolation are probably not significant. A rapid determination of the area-mean base pressure is possible by applying a linear curve fit (when possible) to the measured base pressure distributions of figure 6 and using the expression

$$\bar{p}_b = \frac{2}{3}(p_b)_{r_y/r_b=1} + \frac{1}{3}(p_b)_{r_y/r_b=0} \tag{3}$$

The area-mean base pressures determined from equation (3) were compared with those obtained from equation (2) and found to be in good agreement in most instances, thereby, the assumption of a linear base pressure variation across the base is supported.

The area-mean base pressure can also be expressed, with a linear base pressure variation across the base assumed and with the help of equation (2), as a function of the base pressure corresponding to a given value of r_y/r_b by the relation

$$\bar{p}_b = \frac{(p_b)_{r_y/r_b}}{1 + B\left(\frac{r_y}{r_b} - \frac{2}{3}\right)} \tag{4}$$

where B is the slope of a linear curve fairing to the data of a plot of $p_b/\bar{p}_b$ as a function of r_y/r_b. Examination of equation (4) shows that a base pressure measurement at $\frac{r_y}{r_b} = \frac{2}{3}$ is equal to the area-mean base pressure provided the base-pressure variation across the base is linear; therefore, the base drag of cones may be determined directly from a single base pressure measurement at $\frac{r_y}{r_b} = \frac{2}{3}$ for laminar flow. (For a parabolic distribution across the base, as experienced in the laminar base flow study of reference 4, the area-mean base pressure is equal to a base pressure measurement at $r_y/r_b = 0.7$.)

The effect of Reynolds number, based on model surface length, on the ratio of area-mean base pressure to measured stagnation pressure behind a normal shock at Mach numbers 13.8 and 19.6 is shown in figure 9. At Mach 13.8 (fig. 9(a)), an influence of Reynolds number on the base pressure ratio is observed for the pointed cone, whereas no significant influence of Reynolds number is observed on the base pressure ratio for the spherically blunted cones. At Mach 19.6 (fig. 9(b)), the base pressure ratio is

observed to be dependent on Reynolds number for all bluntness ratios. A summary of the results of figure 9, along with the Mach 10.6 and 15.6 results, is shown in figure 10 where the area-mean base pressure is nondimensionalized by the measured stagnation pressure behind a normal shock in figure 10(a) and by the calculated free-stream static pressure in figure 10(b). Comparison of figures 10(a) and 10(b) shows that for a given Reynolds number and bluntness ratio, normalization by $p_{t,2}$ (fig. 10(a)) tends to reduce the Mach number dependence shown in figure 10(b). An increase in bluntness ratio results in an increase in $\bar{p}_b/p_{t,2}$ and $\bar{p}_b/p_\infty$ for all Mach numbers and Reynolds numbers. For Reynolds numbers greater than 0.1×10^6, $\bar{p}_b/p_{t,2}$ for the spherically blunted cones is relatively insensitive to Reynolds number; whereas, for Reynolds numbers less than 0.1×10^6, $\bar{p}_b/p_{t,2}$ decreases with decreasing Reynolds number for all bluntness ratios. (See fig. 10(a).) This trend (decreasing area-mean base pressure with decreasing Reynolds number) was also observed in the laminar study of reference 4, and is in qualitative agreement with the theoretical findings of reference 26 (based on the laminar mixing between the outer flow, separated shear layer, and the base recirculation region flow (see sketch in fig. 16)).

The data of figure 10 are also plotted in figure 11, where $\bar{p}_b/p_{t,2}$ and $\bar{p}_b/p_\infty$ are shown as functions of free-stream Mach number for the various bluntness ratios. Also shown are existing methods for predicting base pressure on axisymmetric bodies at hypersonic Mach numbers (fig. 11(b)). The scarcity of existing methods for the present Mach numbers is apparent and is primarily due to the extremely complex nature of the separated flow over the base region. The solid line of figure 11(b) denotes a theoretical prediction for a 10° semiapex angle pointed cone having laminar boundary layer and zero base heat transfer as tabulated in reference 27 and the dash lines represent turbulent boundary-layer semiempirical predictions (method of ref. 28) for 9° semiapex angle cones having bluntness ratios of 0 and 0.8. The predictions for Mach numbers greater than 10 and for a bluntness ratio of 0.8 were obtained from the author of reference 28. The measured pointed-cone values at Mach 10.6, at Mach 13.8 for the highest Reynolds number, and at Mach 19.6 for the lowest Reynolds numbers are observed to be in good agreement with the turbulent semiempirical prediction of reference 28, whereas the remaining pointed-cone data are in reasonably good agreement with the laminar theoretical prediction of reference 27. Since reference 25 shows that a laminar boundary layer and near wake should exist for the present results and figure 9 shows the base pressure for the pointed cone to be dependent on Reynolds number for Mach 13.8 and 19.6, the agreement between some of the present pointed-cone results and the turbulent prediction of reference 28 is believed to be fortuitous and results from the dependence of $\bar{p}_b/p_\infty$ on Reynolds number for the pointed cone.

The value of $\bar{p}_b/p_\infty$ for a bluntness ratio of 0.8 was always greater than 1 for the present Mach numbers (fig. 11(b)) and thereby corresponds to a positive base pressure

coefficient. This trend $(p_b > p_\infty)$ was predicted by Ferri and Pallone (ref. 29) as early as 1956 and has been observed in the recent experimental results of references 9, 11, and 12.

References 2, 5, 11, 26, 28, and 29 have shown that base pressure is governed largely by the local flow conditions immediately ahead of the model base. The present area-mean base pressures, nondimensionalized by the calculated inviscid local model surface pressure immediately ahead of the model base, are plotted as a function of calculated inviscid local Reynolds number (fig. 12(a)) and calculated inviscid local Mach number (fig. 12(b)). The calculated inviscid conditions were obtained from the ideal-gas flow-field solutions of reference 30. For the spherically blunted cones, $\bar{p}_b/p_L$ is relatively insensitive to local Reynolds number for local Reynolds numbers greater than 0.01×10^6; whereas, for local Reynolds numbers less than 0.01×10^6, $\bar{p}_b/p_L$ decreases with decreasing local Reynolds number. Although there appears to be no correlation of results in terms of local Reynolds number, the results in terms of the local Mach number appear to correlate reasonably well (fig. 12(b)). Shown in figure 12(b), along with the present data, is the turbulent boundary-layer correlation curve of reference 28 which was obtained from flight-test data for full-scale flight vehicles having various bluntness ratios. With turbulent boundary layers, $\bar{p}_b/p_\infty$ for a given configuration and Mach number becomes essentially independent of variation in Reynolds number and thus tends toward a substantially constant level (ref. 2). Hence, the correlation of reference 28, as shown in figure 12(b), may be used to predict $\bar{p}_b/p_\infty$ for a given configuration and Mach number. Due to the Reynolds number dependence for the laminar-boundary-layer case, this procedure is not applicable to the present results for the entire Reynolds number range. However, by restricting the Reynolds number so that $0.1 \times 10^6 \leq R_{\infty,s} \leq 1 \times 10^6$, the curve fairing to the present data of figure 12(b) can be used, in conjunction with the flow-field solutions of reference 30 and relations of reference 21, to predict $\bar{p}_b/p_{t,2}$ and $\bar{p}_b/p_\infty$ for a given configuration and Mach number as shown in figure 13. The predicted values of $\bar{p}_b/p_{t,2}$ (fig. 13(a)) and $\bar{p}_b/p_\infty$ (fig. 13(b)) for the spherically blunted cones are in reasonable agreement with the measured base pressure results for $R_{\infty,s} > 0.1 \times 10^6$ and show that $\bar{p}_b/p_{t,2}$ decreases and $\bar{p}_b/p_\infty$ increases with increasing Mach number in this Reynolds number range. The discrepancies observed between the predicted base pressure ratios and measured base pressure results for the pointed cone are believed to be due to a Reynolds number dependence; hence, the present method for predicting base pressure ratios for pointed cones should be used with caution. Since the present method of predicting laminar base pressure ratio and the method of reference 28 for predicting turbulent base pressure ratio are based on a correlation in terms of p_L and M_L, the present method should prove applicable for a range of cone semiapex angle as well as of Mach number and bluntness ratio as was the case in reference 28.

Attempts were made to correlate the present results, over the entire range of Reynolds number, in terms of local conditions, by plotting $\bar{p}_b/p_L$ as a function of $M_L/\sqrt{R_{L,s}}$ as suggested in reference 10, $\bar{p}_b/p_L$ as a function of $M_L\sqrt{\mu_w T_L/\mu_L T_w R_{L,s}}$, and $\bar{p}_b/p_L$ as a function of $\sqrt{R_{L,s}}/M_L^2$ as suggested in reference 4; all these attempts met with little success.

Base Drag

The base drag contribution to the estimated total inviscid drag for the configurations of the present investigation is shown in figure 14, where drag coefficient is plotted as a function of free-stream Mach number. Forebody drag coefficients were computed by using equation (3) of reference 31 in conjunction with the tables of Newtonian aerodynamic coefficients for conic and spheric bodies of reference 32 and are represented in figure 14 by the dash lines. (A maximum pressure coefficient of 2 was employed for the Newtonian theory calculations.) Also shown in figure 14 are results from reference 7 for 9^o semi-apex angle cones having bluntness ratios of 0 and 0.286. The results of reference 7 show the pointed-cone base drag coefficient to be approximately 57 percent of the total drag coefficient at a Mach number of 3.5 and 19 percent at a Mach number of 9.2. The present pointed-cone results show the base drag coefficient to be approximately 15 percent of the total drag coefficient at a Mach number of 10.6 and approximately 2 to 4 percent at a Mach number of 19.6. For a bluntness ratio of 0.286, the results of reference 7 show the base drag coefficient to be approximately 41 percent of the total drag coefficient at a Mach number of 3.5 and 7 percent at a Mach number of 9.2. The present results for a bluntness ratio of 0.3 show that the base drag coefficient represents approximately 5 percent of the total drag coefficient at a Mach number of 10.6 and less than 2.5 percent for Mach numbers from 13.8 to 19.6. The base drag coefficient was less than approximately 2 percent of the total drag coefficient for bluntness ratios of 0.55 and 0.8 for the present Mach numbers.

Sting Pressure Distributions

Static-pressure distributions along the sting having $D/d_b = 0.583$ are shown in figure 15 for the various models. In general, the sting surface pressure ratio increases downstream of the base plane to a maximum level corresponding to the region where the separated flow is assumed to reattach to the sting surface. The ratio of sting surface pressure to free-stream static pressure in this recompression region is observed to increase with increasing free-stream Mach number for all bluntness ratios; this variation agrees with the trends of free-stream base pressure ratio. After recompression the sting surface pressure ratio is observed to decrease toward free-stream static pressure.

Dividing-Streamline Turning Angle

Estimation of the dividing-streamline turning angle (defined in the sketch in fig. 16, which does not illustrate the presence of a sting) from the sting surface pressure distributions of figure 15 is difficult primarily because of the arbitrary nature by which the most upstream point of the recompression region can be defined. To estimate the dividing-streamline turning angle more accurately, tuft studies were made with the tufts positioned along the sting having $D/d_b = 0.583$ as shown in figure 5(a). The most upstream tuft indicating a rearward deflection during a tunnel test was assumed to indicate the point of attachment of the streamline dividing the separated boundary layer from the flow in the recirculation region. As shown in the sketch (fig. 16), the dividing streamline was assumed to be straight. The results derived from the present tuft study are shown in figure 16 where the turning angle, as determined from the tuft deflections, is plotted as a function of free-stream Mach number. The uncertainty involved in determining the point of attachment is indicated by the barred lines through the symbols in figure 16. Also shown in figure 16 are results obtained from a study of ballistic-range shadowgraphs as presented in reference 33.

From figure 16, the present turning angle is observed to be approximately constant for the pointed cone and the spherically blunted cone having a bluntness ratio of 0.8 for Mach numbers from approximately 10.5 to 20. The turning angles for the pointed cone are observed to be greater than those determined for the 0.8 spherically blunted cone throughout the present Mach number range. The results of reference 9 show that the rear stagnation point (defined in sketch in fig. 16) for a free-flight or wire-supported 10° semiapex angle pointed cone at a Mach number of 12.8 corresponds to $\beta = 44^\circ$. As discussed in reference 33, the rear stagnation-point location can be inferred from the trailing wake shock origin. Reference 33 shows that the rear stagnation point for a 9° semiapex angle pointed cone corresponds to $\beta \approx 44^\circ$ for a Mach number of 10.5 and $\beta \approx 35^\circ$ to 38° for Mach numbers of 13 to 17. The results of reference 8, where a wire-supported 5° semiapex angle pointed cone was tested at free-stream Mach numbers of 8 and 11.8, showed a rear stagnation point corresponding to $\beta = 36^\circ$. The present pointed-cone data of figure 16 show an inferred rear stagnation-point location corresponding to $\beta \approx 44^\circ$ for the present Mach number range and hence is in reasonable agreement with the pointed-cone results of references 8, 9, and 33. However, the effect of the sting on the present tuft results is not known and the agreement with the stingless studies of references 8, 9, and 33 may be coincidental.

CONCLUSIONS

Base pressure measurements were obtained in the Langley hotshot tunnel at an angle of attack of 0° for a series of cones having semiapex angles of 9° and bluntness

ratios of 0, 0.3, 0.55, and 0.8. Nominal free-stream Mach numbers were 10.6, 13.8, 15.6, and 19.6; free-stream Reynolds numbers, based on model surface length, were approximately 0.02×10^6 to 2×10^6 in nitrogen; and laminar boundary-layer flow was assumed. Results of the study led to the following conclusions:

1. Base pressure measurements obtained 0.21 to 0.83 base radius from the model axis showed the existence of radial base pressure gradients for all bluntness ratios over the entire Mach number and Reynolds number range, with the base pressure increasing toward the model axis. The existence of a radial base pressure gradient is in agreement with several other investigations having laminar boundary-layer and near-wake flow but in opposition to those having transitional or turbulent boundary-layer and near-wake flow.

2. The ratio of area-mean base pressure to stagnation pressure behind a normal shock for the spherically blunted cones was relatively insensitive to Reynolds number for Reynolds numbers greater than 0.1×10^6 but decreased with decreasing Reynolds number for Reynolds numbers less than 0.1×10^6 for all bluntness ratios. This area-mean base pressure ratio increased with decreasing Mach number and increasing bluntness ratio.

3. A semiempirical method for estimating the laminar base pressure ratio of spherically blunted cones in hypersonic flow for Reynolds numbers, based on model surface length, from 0.1×10^6 to 1×10^6 was found to yield reasonable agreement with the present measured base pressure results.

4. The contribution of base drag to total inviscid drag decreased with increasing bluntness ratio and increasing Mach number. The base drag was less than approximately 2 percent of the total inviscid drag for bluntness ratios of 0.55 and 0.8 over the entire Mach number range but was approximately 15 percent for the pointed cone and approximately 5 percent for the 0.3 spherically blunted cone at a Mach number of 10.6.

Langley Research Center,
National Aeronautics and Space Administration,
Langley Station, Hampton, Va., June 10, 1968,
129-01-03-07-23.

REFERENCES

1. Kavanau, L. L.: Results of Some Base Pressure Experiments at Intermediate Reynolds Numbers With M = 2.84. Rep. No. HH-150-117 (Contract N7-onr-295-Task 3), Inst. Eng. Res., Univ. of California, Oct. 22, 1953.

2. Whitfield, Jack D.; and Potter, J. Leith: On Base Pressures at High Reynolds Numbers and Hypersonic Mach Numbers. AEDC-TN-60-61, U.S. Air Force, Mar. 1960.

3. Roffe, G.; Fruchtman, I.; and Linger, S.: Measurements of Wall Temperature Effects on Base Flow. Tech. Rep. No. 490 (Contract SD-149), Gen. Appl. Sci. Lab., Inc., Dec. 1964. (Available from DDC as AD 455 974.)

4. Kavanau, L. L.: Base Pressure Studies in Rarefied Supersonic Flows. Rep. No. HB-150-125 (Contract N7-onr-295-Task 3), Inst. Eng. Res., Univ. of California, Nov. 1, 1954.

5. Chapman, Dean R.: An Analysis of Base Pressure at Supersonic Velocities and Comparison With Experiment. NACA Rep. 1051, 1951. (Supersedes NACA TN 2137.)

6. Reller, John O., Jr.; and Hamaker, Frank M.: An Experimental Investigation of the Base Pressure Characteristics of Nonlifting Bodies of Revolution at Mach Numbers From 2.73 to 4.98. NACA TN 3393, 1955. (Supersedes NACA RM A52E20.)

7. Zarin, Neil A.: Base Pressure Measurements on Sharp and Blunt 9^{o} Cones at Mach Numbers From 3.50 to 9.20. Mem. Rep. No. 1709, Ballistic Res. Lab., Aberdeen Proving Ground, Nov. 1965.

8. Zakkay, Victor; and Cresci, Robert J.: An Experimental Investigation of the Near Wake of a Slender Cone at $M_{\infty} = 8$ and 12. AIAA J., vol. 4, no. 1, Jan. 1966, pp. 41-46.

9. Muntz, E. P.; and Softley, B. J.: An Experimental Study of Laminar Near Wakes. BSD-TR 65-314, U.S. Air Force, June 1965. (Available from DDC as AD 467 080.)

10. Lockman, William K.: Free-Flight Base Pressure and Heating Measurements on Sharp and Blunt Cones in a Shock Tunnel. AIAA J. (Tech. Notes), vol. 5, no. 10, Oct. 1967, pp. 1898-1900.

11. Miller, Charles G., III: An Experimental Investigation of Support Interference on a Blunt Body of Revolution at a Mach Number of Approximately 20. NASA TN D-2742, 1965.

12. Cassanto, John M.: Radial Base-Pressure Gradients in Laminar Flow. AIAA J. (Tech. Notes), vol. 5, no. 12, Dec. 1967, pp. 2278-2279.

13. Mechtly, E. A.: The International System of Units – Physical Constants and Conversion Factors. NASA SP-7012, 1964.

14. Miller, Charles G., III; Creel, Theodore R., Jr.; and Smith, Fred M.: Calibration Experience in the Langley Hotshot Tunnel for Mach Numbers From 12 to 26. NASA TN D-3278, 1966.

15. Smotherman, W. E.: A Miniature Wafer-Style Pressure Transducer. AEDC-TR-60-11, U.S. Air Force, Oct. 1960.

16. Grabau, Martin; Humphrey, Richard L.; and Little, Wanda J.: Determination of Test-Section, After-Shock, and Stagnation Conditions in Hotshot Tunnels Using Real Nitrogen at Temperatures From 3000 to 4000° K. AEDC-TN-61-82, U.S. Air Force, July 1961.

17. Erickson, Wayne D.: Vibrational-Nonequilibrium Flow of Nitrogen in Hypersonic Nozzles. NASA TN D-1810, 1963.

18. Hurle, I. R.; Russo, A. L.; and Hall, J. Gordon: Experimental Studies of Vibrational and Dissociative Nonequilibrium in Expanded Gas Flows. [Preprint] 64-439, Amer. Inst. Aeronaut. Astronaut., Aug. 1963.

19. Guy, R. W.; and Winebarger, R. M.: Effect of Orifice Size and Heat-Transfer Rate on Measured Static Pressures in a Low-Density Arc-Heated Wind Tunnel. NASA TN D-3829, 1967.

20. Smotherman, W. E,; and Maddox, W. V.: Variable Reluctance Pressure Transducer Development. AEDC-TDR-63-135, U.S. Air Force, July 1963.

21. Ames Research Staff: Equations, Tables, and Charts for Compressible Flow. NACA Rep. 1135, 1953. (Supersedes NACA TN 1428.)

22. Harvey, William D.: Effects of Leading-Edge Bluntness on Pressure and Heat-Transfer Measurements Over a Flat Plate at a Mach Number of 20. NASA TN D-2846, 1965.

23. Griffith, B. J.; and Weddington, E. D.: Recent Refinements and Advancements of Hypersonic Testing Techniques in the 100-Inch Tunnel F of the Von Karman Gas Dynamics Facility. Fourth Hypervelocity Techniques Symposium, Univ. of Denver and Arnold Eng. Develop. Center, Nov. 1965, pp. 485-527.

24. Fay, J. A.; and Riddell, F. R.: Theory of Stagnation Point Heat Transfer in Dissociated Air. J. Aeronaut. Sci., vol. 25, no. 2, Feb. 1958, pp. 73-85, 121.

25. Waldbusser, Edwin: Shape Effects on Hypersonic Slender Body Wake Geometry and Transition Distance. J. Spacecraft Rockets, vol. 4, no. 5, May 1967, pp. 657-662.

26. Crocco, Luigi; and Lees, Lester: A Mixing Theory for the Interaction Between Dissipative Flows and Nearly Isentropic Streams. J. Aeronaut. Sci., vol. 19, no. 10, Oct. 1952, pp. 649-676.

27. King, Hartley H.: A Tabulation of Base Flow Properties for Cones and Wedges. EOS Res. Note No. 17 (Contract No. DA-04-495-AMC-28-(Z)), Electro-Opt. Syst., Inc., Jan. 1964. (Available from DDC as AD 426 983.)

28. Cassanto, John M.: Ratio on Base Pressure. AIAA J. (Tech. Notes), vol. 3, no. 12, Dec. 1965, pp. 2351-2352.

29. Ferri, Antonio; and Pallone, Adrian: Note on the Flow Fields on the Rear Part of Blunt Bodies in Hypersonic Flow. WADC Tech. Note 56-294, U.S. Air Force, July 1956.

30. Roberts, J. F.: Lewis, Clark H.; and Reed, Marvin: Ideal Gas Spherically Blunted Cone Flow Field Solutions at Hypersonic Conditions. AEDC-TR-66-121, U.S. Air Force, Aug. 1966.

31. Harris, Julius E.: Force-Coefficient and Moment-Coefficient Correlations and Air-Helium Simulation for Spherically Blunted Cones. NASA TN D-2184, 1964.

32. Wells, William R.; and Armstrong, William O.: Tables of Aerodynamic Coefficients Obtained From Developed Newtonian Expressions for Complete and Partial Conic and Spheric Bodies at Combined Angles of Attack and Sideslip With Some Comparisons With Hypersonic Experimental Data. NASA TR R-127, 1962.

33. Waldbusser, E.: Geometry of the Near Wake of Pointed and Blunt Hypersonic Cones. AIAA J. (Tech. Notes), vol. 4, no. 10, Oct. 1966, pp. 1874-1876.

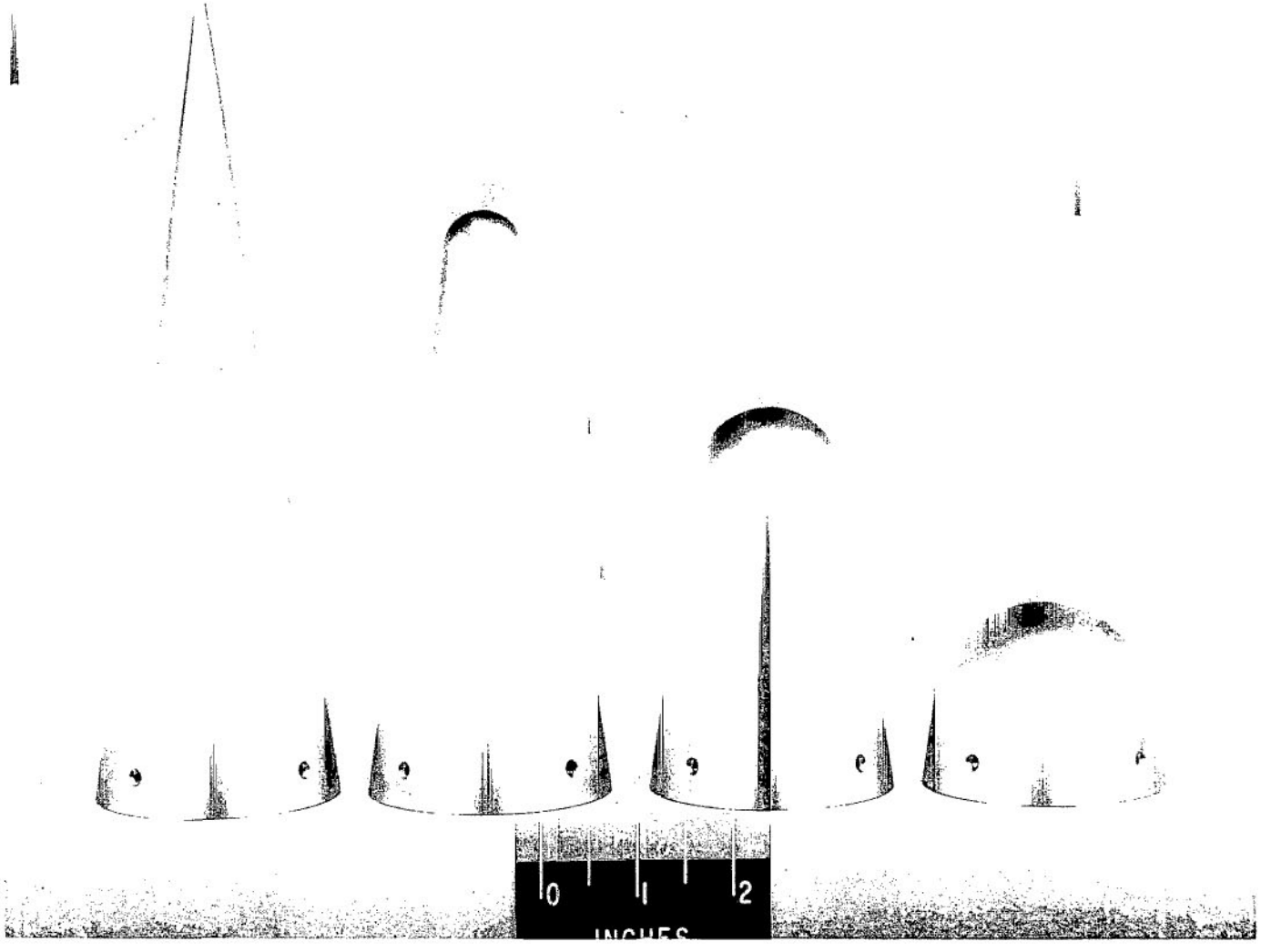

Figure 1.- Series of 9° semiapex angle cone forebodies corresponding to model bluntness ratios of 0, 0.3, 0.55, and 0.8. L-64-10,069

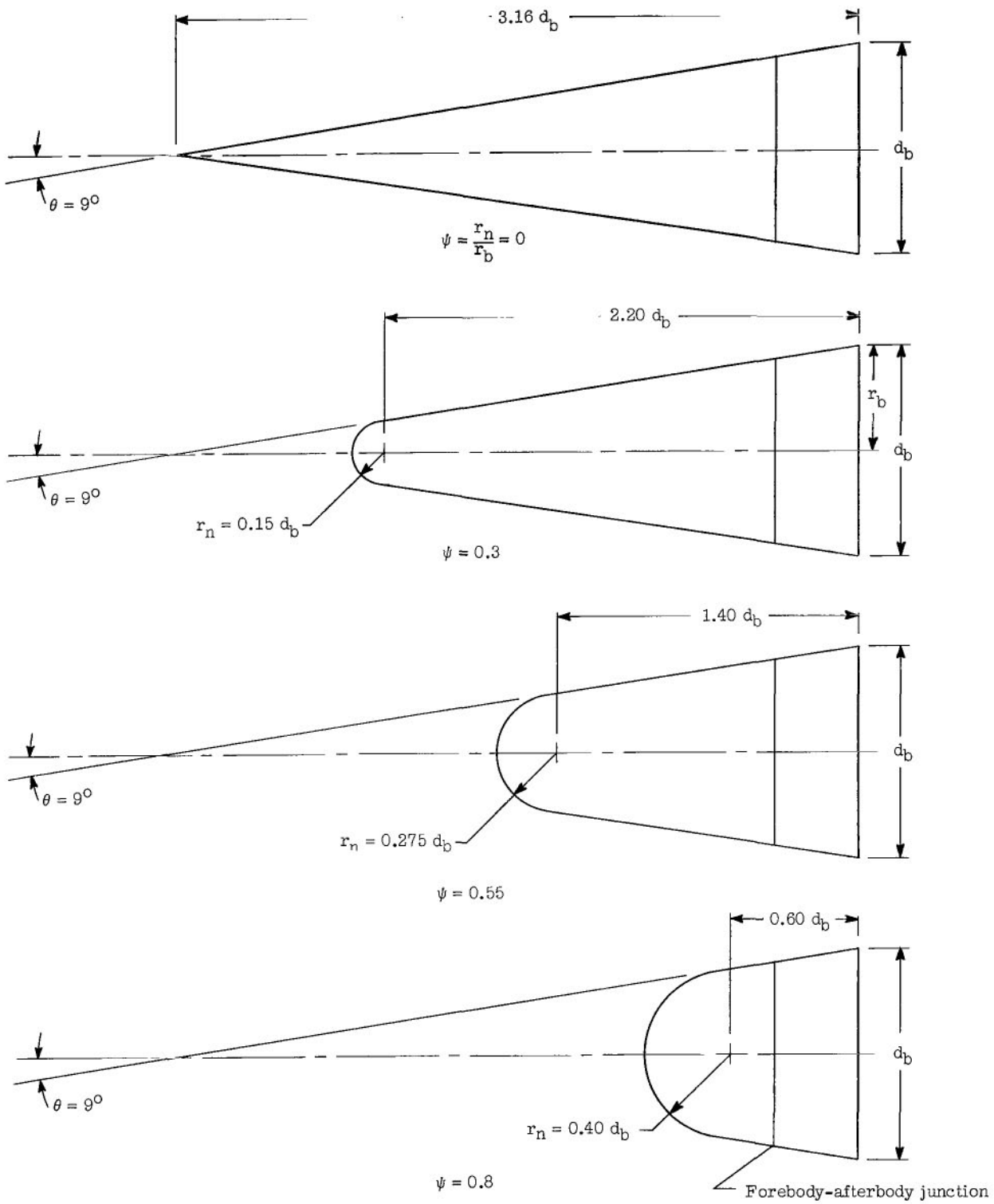

Figure 2.- Model drawings and dimensions. ($d_b = 2r_b = 3$ in. (7.62 cm).)

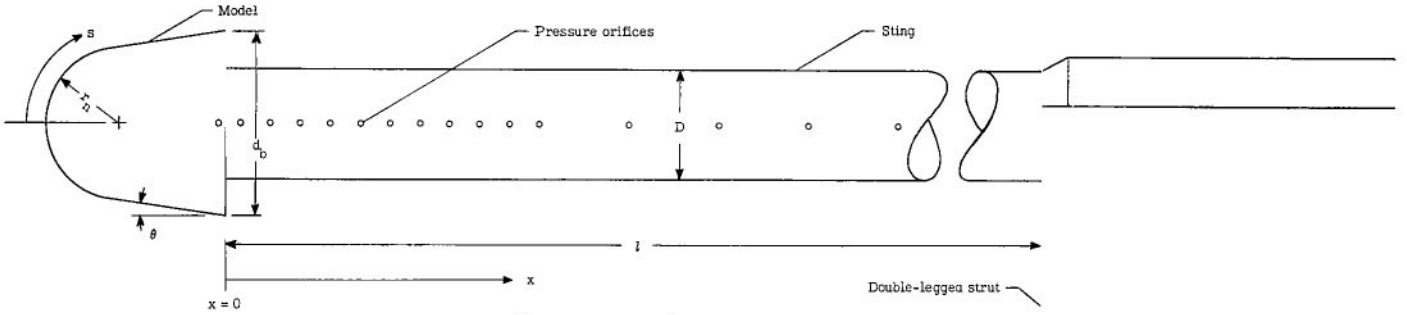

Sting B $(D/d_b = 0.583,\ l/d_b = 12)$

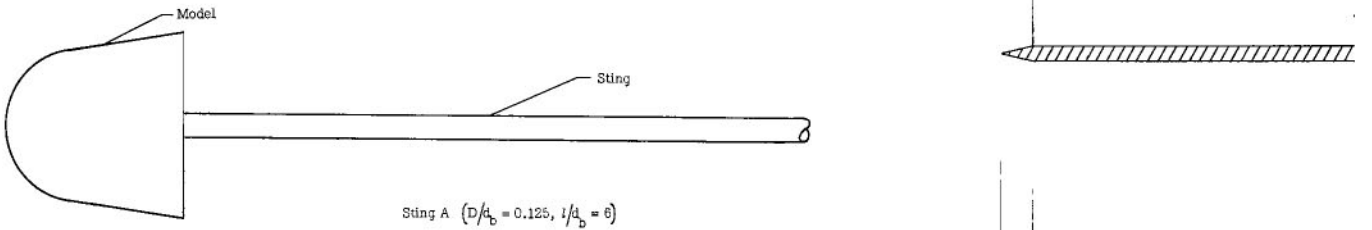

Sting A $(D/d_b = 0.125,\ l/d_b = 6)$

PRESSURE ORIFICE LOCATIONS

Gage location	x/d_b	D/d_b
Model surface	-0.042	0.583
Model base	0	0.125, 0.583
Sting B	.083	0.583
	.250	
	.417	
	.583	
	.750	
	.917	
	1.083	
	1.250	
	1.417	
	1.583	
	1.750	
	2.250	
	2.750	
	3.250	
	3.750	

All pressure orifices 0.022 d_b i.d.

(a) Support arrangements.

Figure 3.- Sketches illustrating support arrangements, model bases, and instrumentation locations. $(d_b = 2r_b = 3$ in. (7.62 cm).)

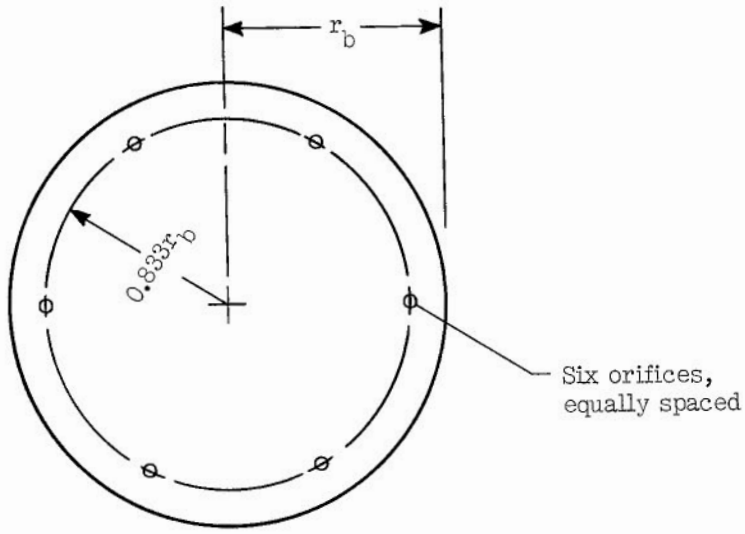

Model base B

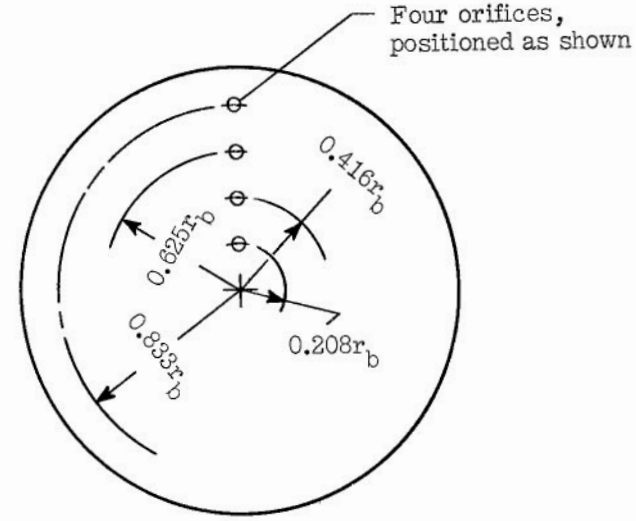

Model base A

(b) Model bases.

Figure 3.- Concluded.

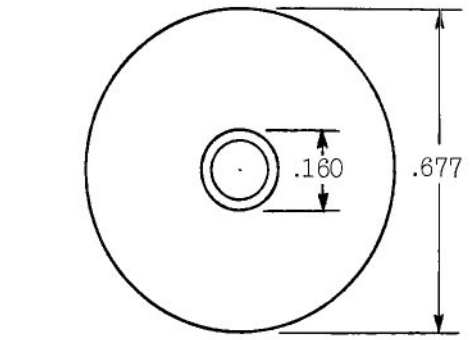

Top view

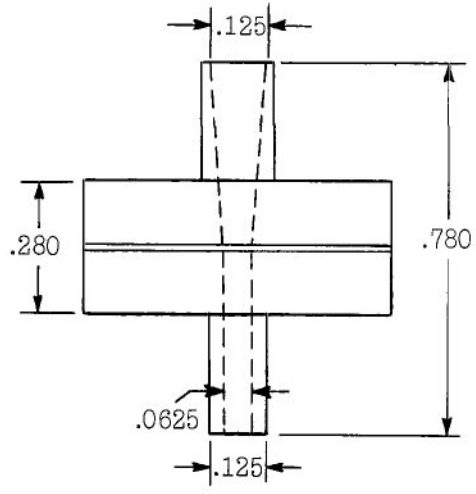

Side view

(a) Geometric detail (dimensions in inches).

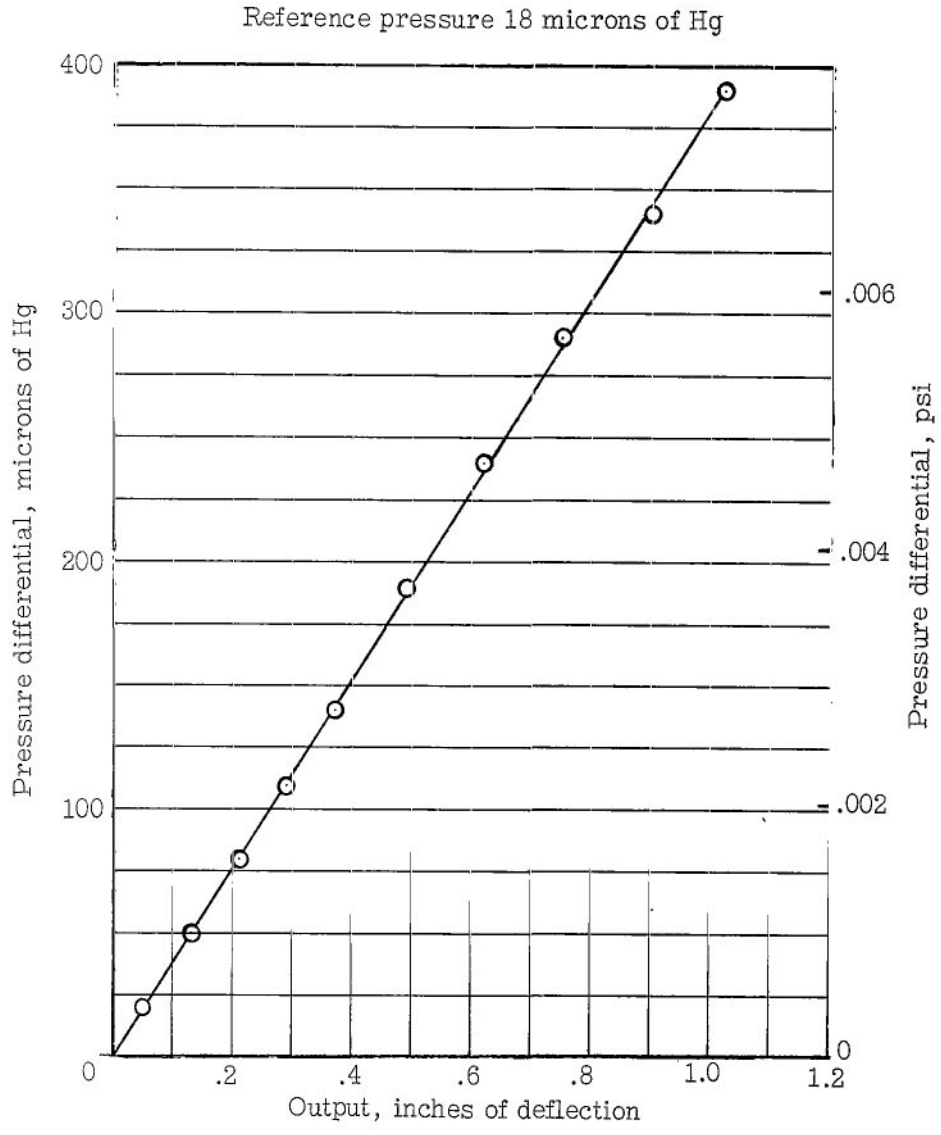

(b) Typical calibration curve.

Figure 4.- Variable reluctance barrel-type pressure transducer. This figure is taken directly from reference 11. (1 in. = 2.54 cm.)

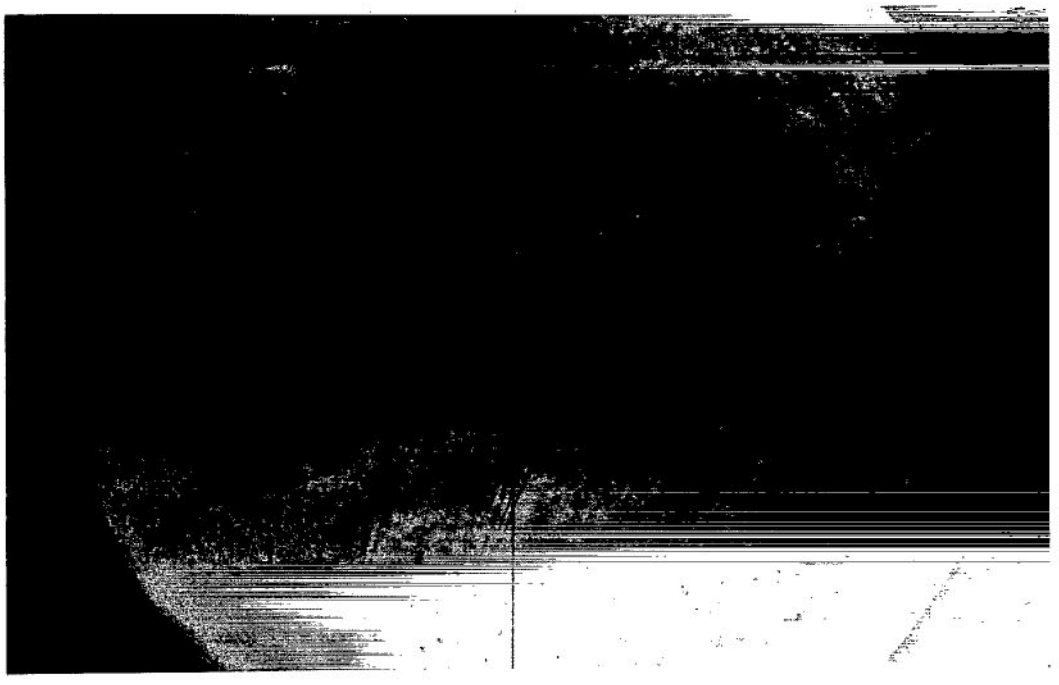

(a) No flow.

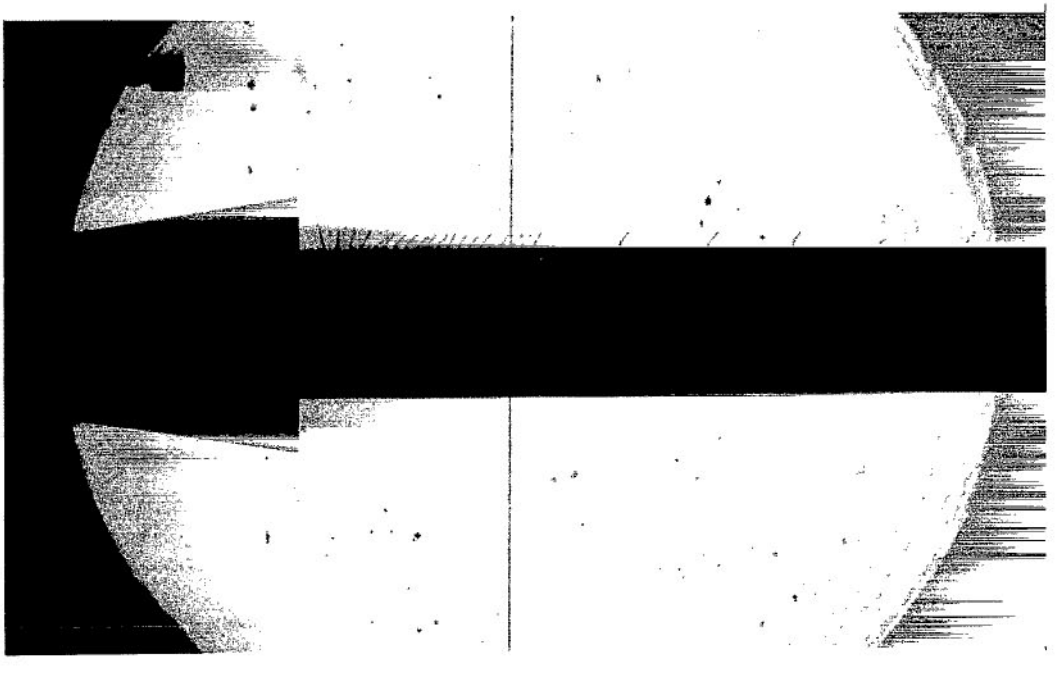

(b) Flow.

L-68-5646

Figure 5.- Representative schlieren photographs illustrating tuft deflections for pointed cone at $M_\infty \approx 17$.

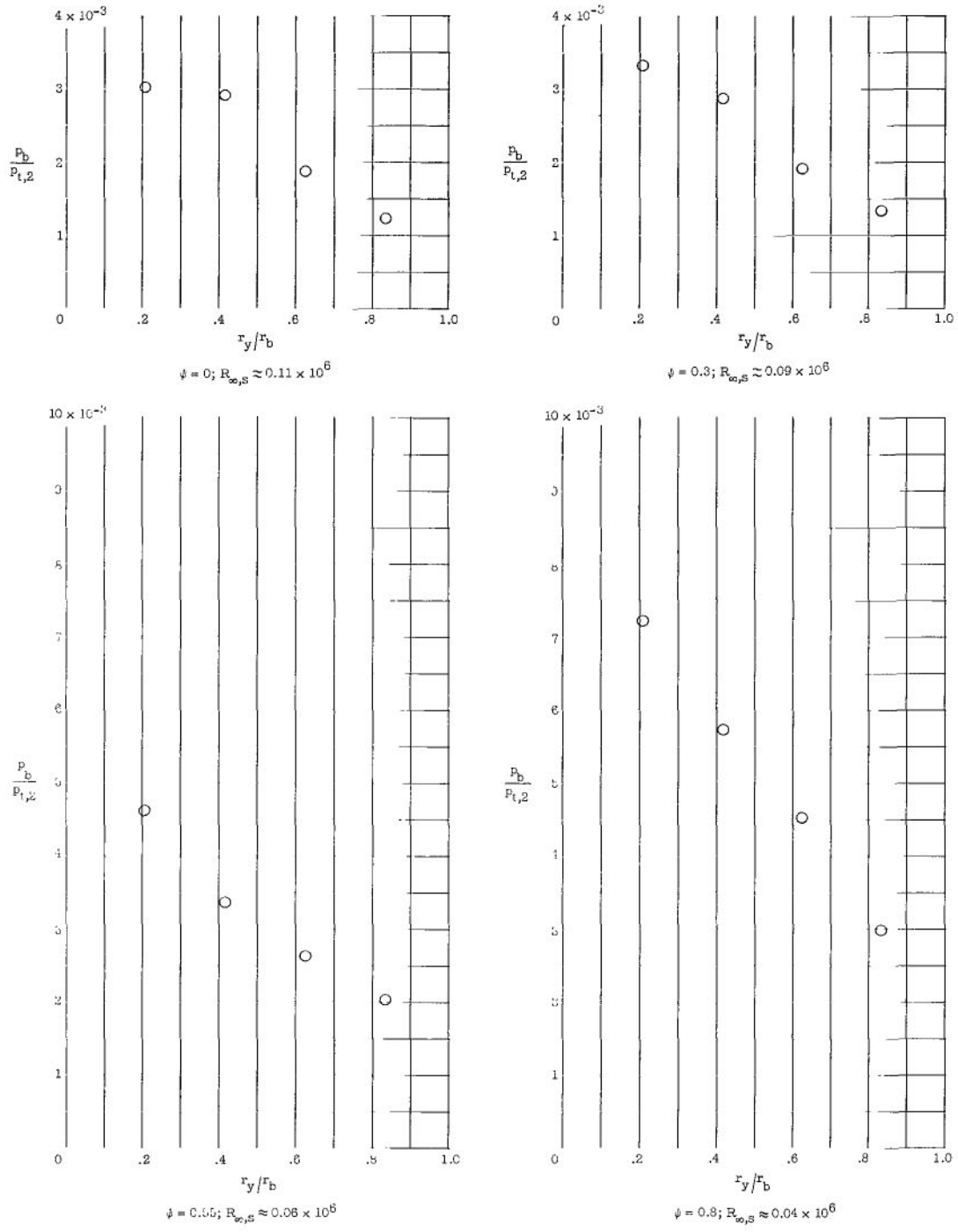

(a) $M_\infty \approx 10.6$.

Figure 6.- Radial base pressure distributions on 9° cones of various bluntness ratios for range of Mach number and Reynolds number. $(t/d_b = 6;\ D/d_b = 0.125.)$

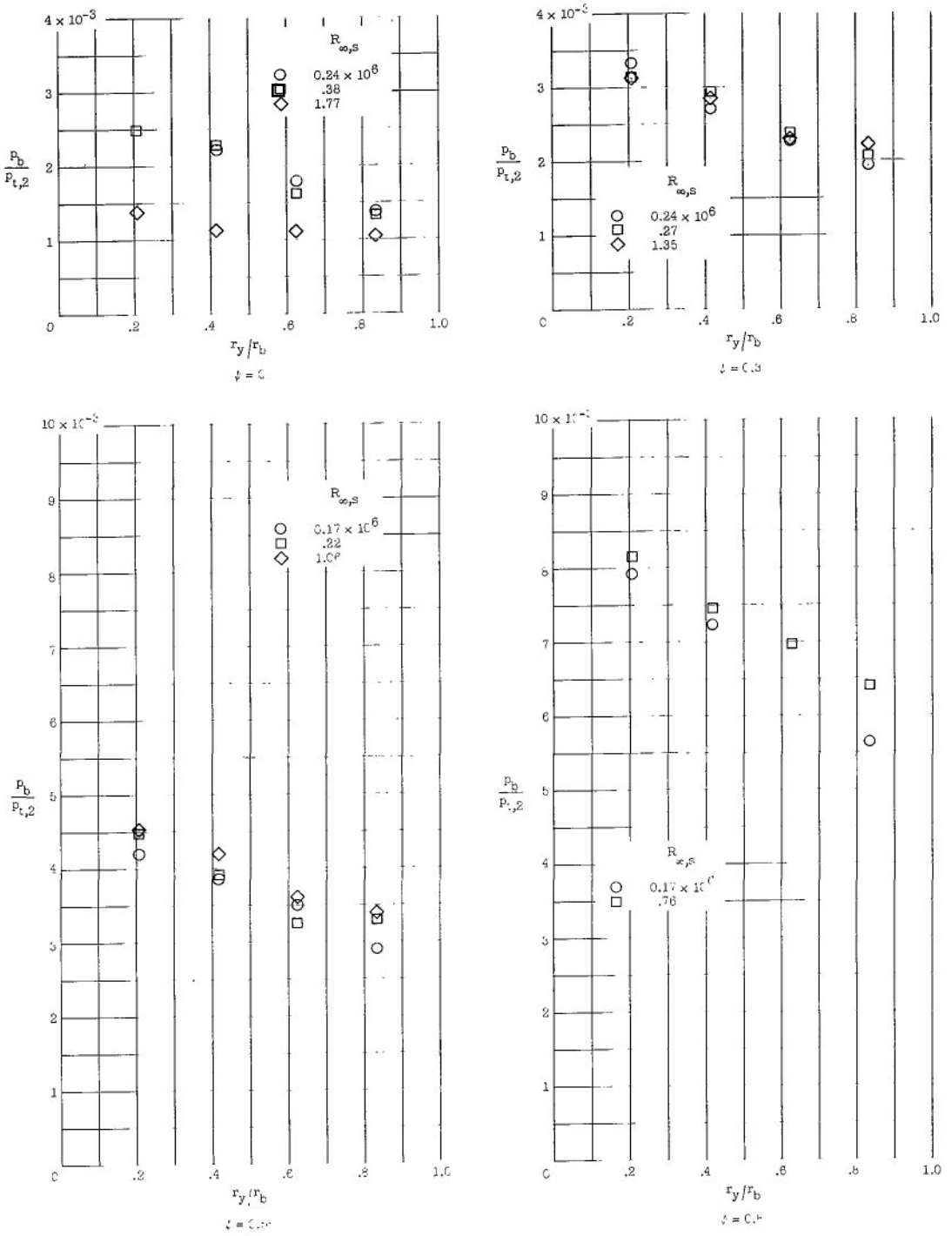

(b) $M_\infty \approx 13.8$.

Figure 6.- Continued.

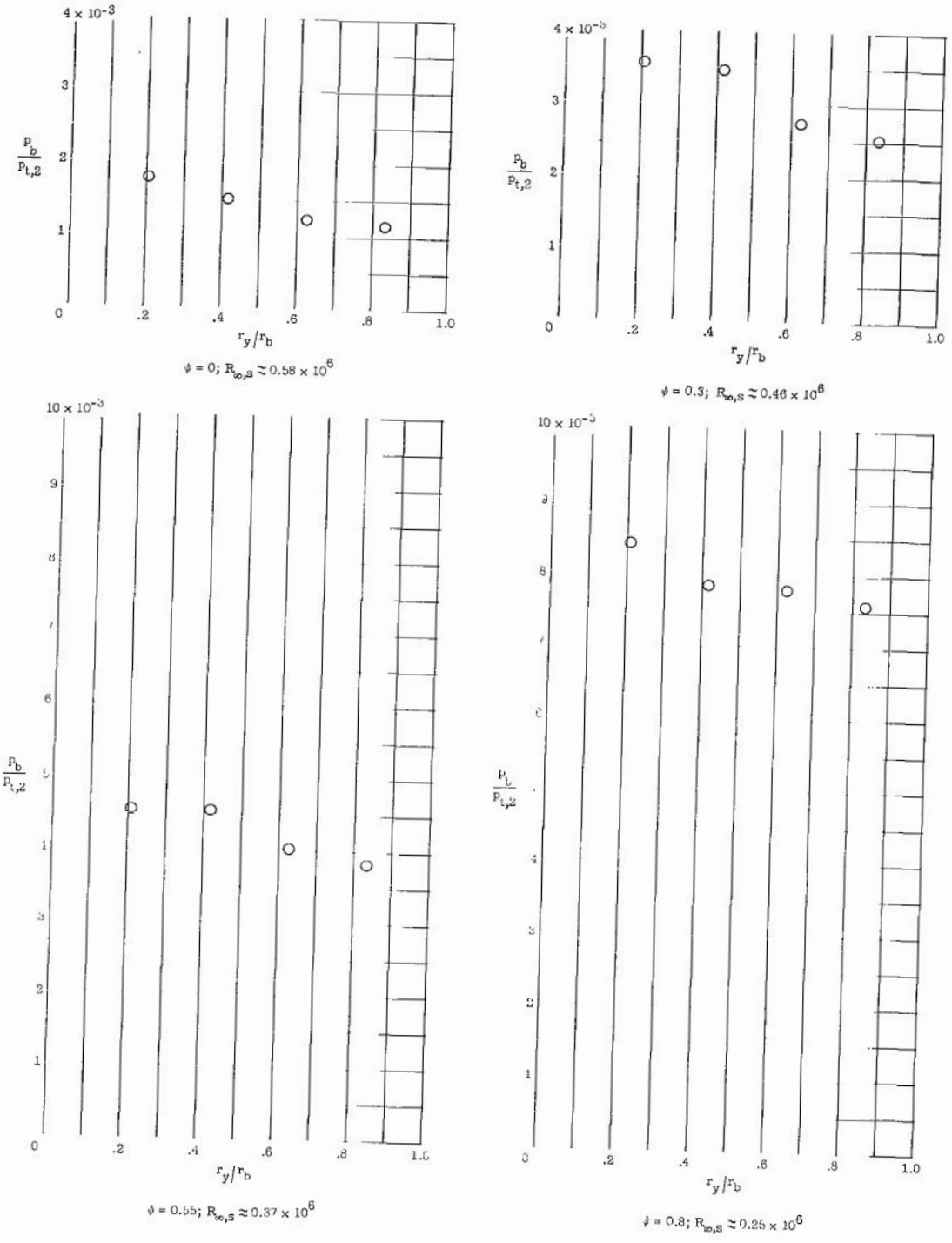

(c) $M_\infty \approx 15.6$.

Figure 6.- Continued.

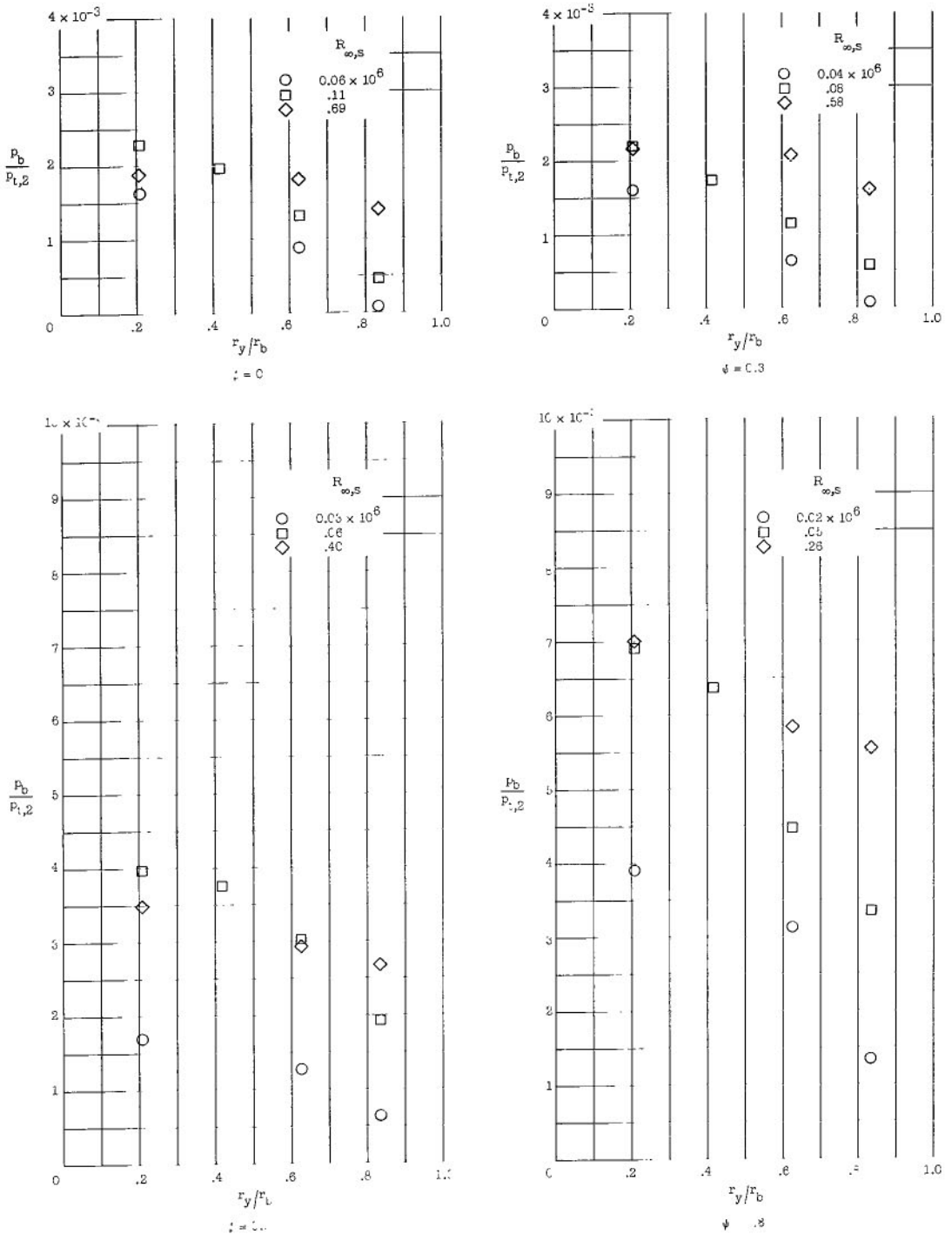

(d) $M_\infty \approx 19.6$.

Figure 6.- Concluded.

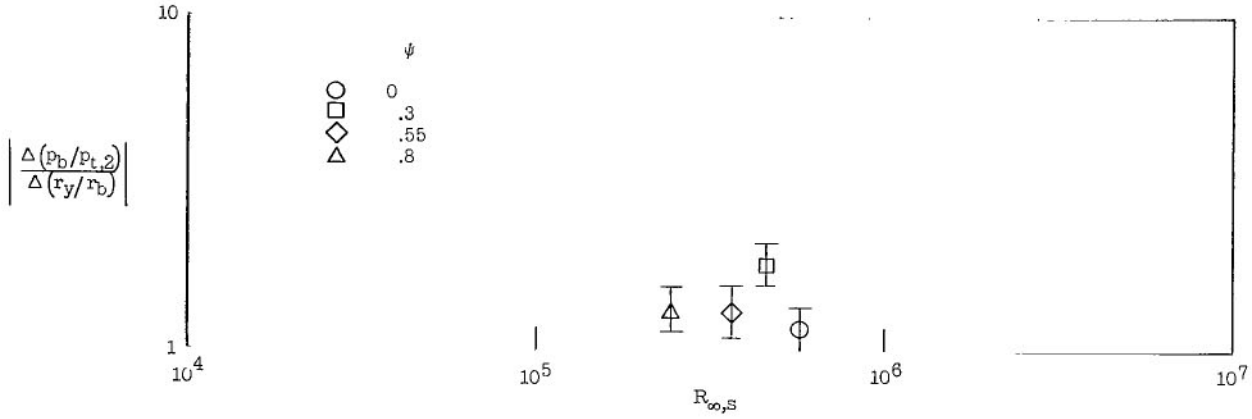

(a) $M_\infty \approx 10.6$.

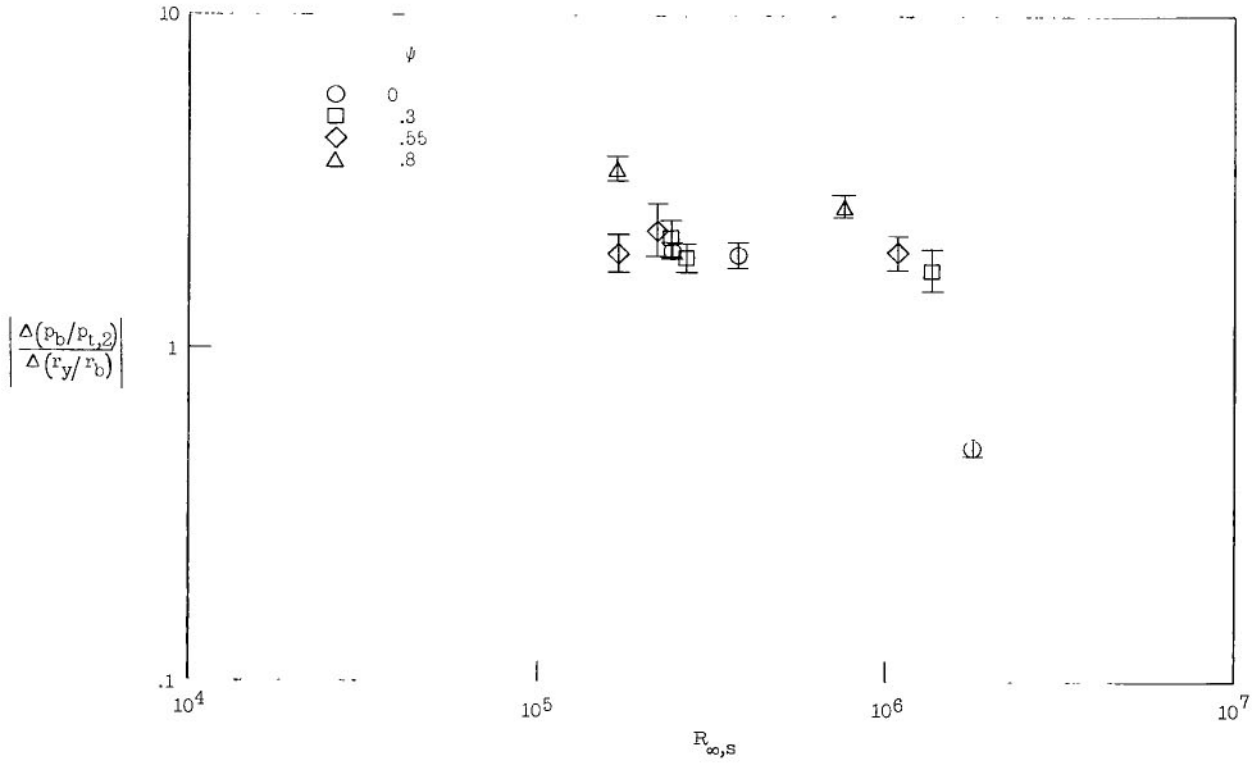

(b) $M_\infty \approx 13.8$.

Figure 7.- Radial base pressure gradient as function of Reynolds number for various bluntness ratios and Mach numbers.

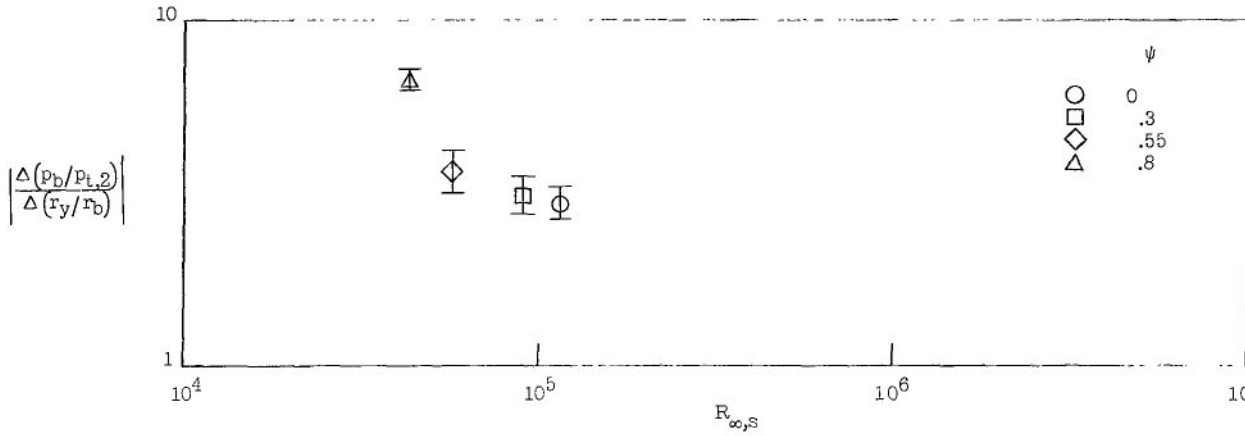

(c) $M_\infty \approx 15.6$.

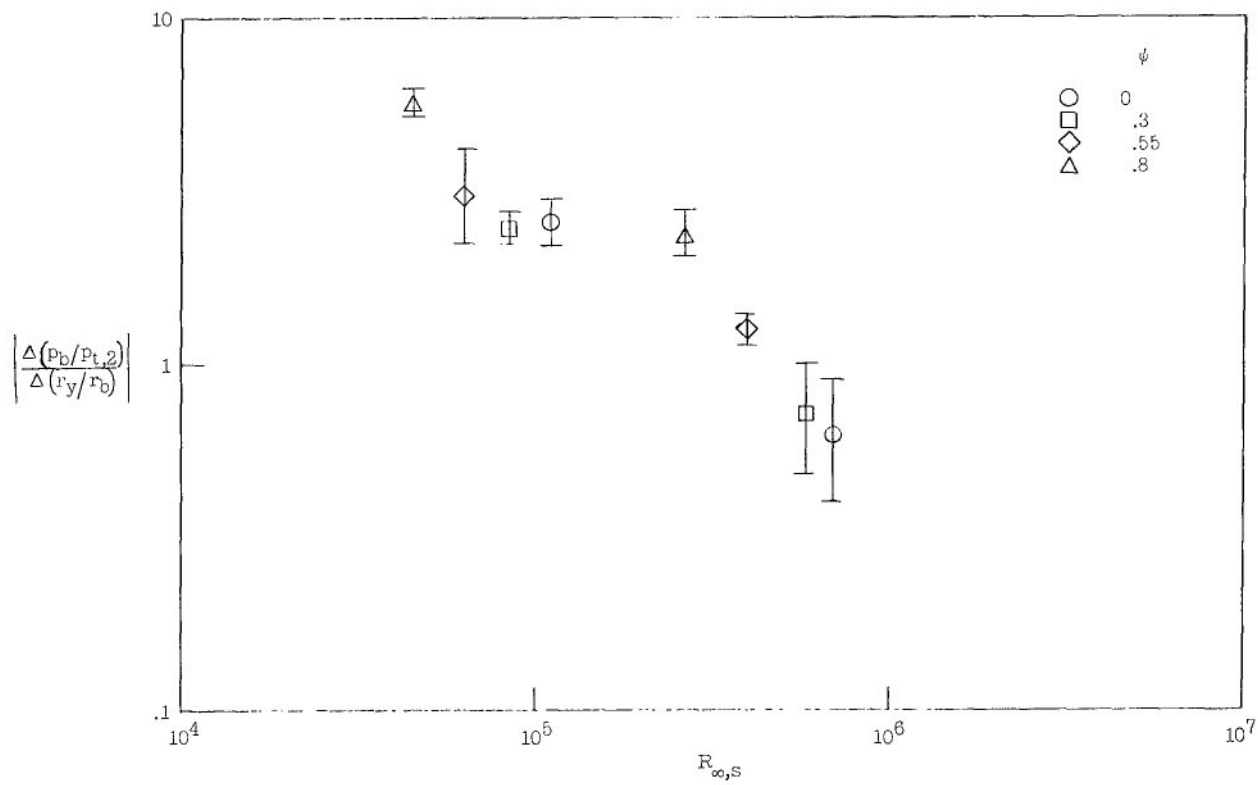

(d) $M_\infty \approx 19.6$.

Figure 7.- Concluded.

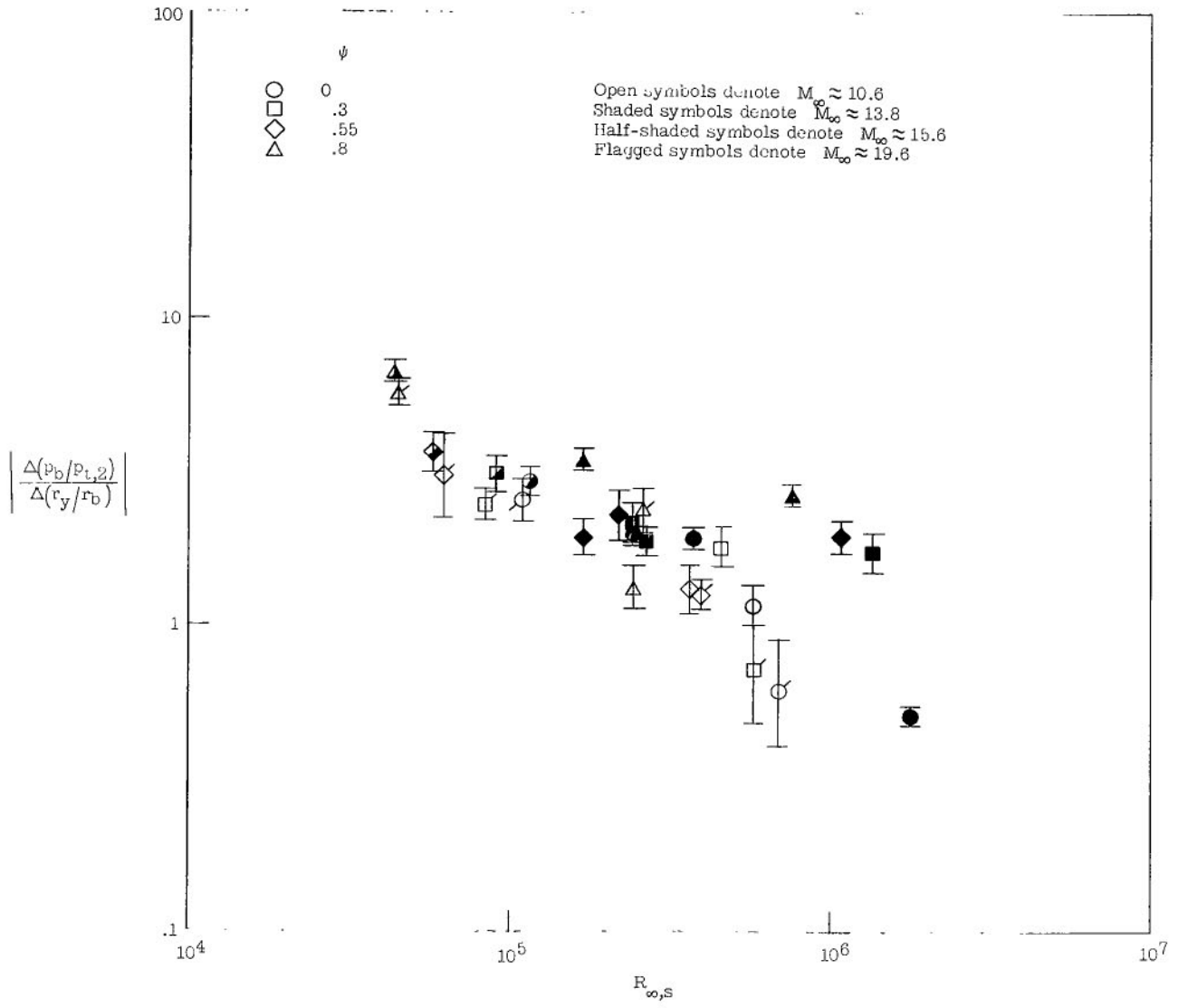

Figure 8.- Radial base pressure gradient as function of Reynolds number for various bluntness ratios and Mach numbers.

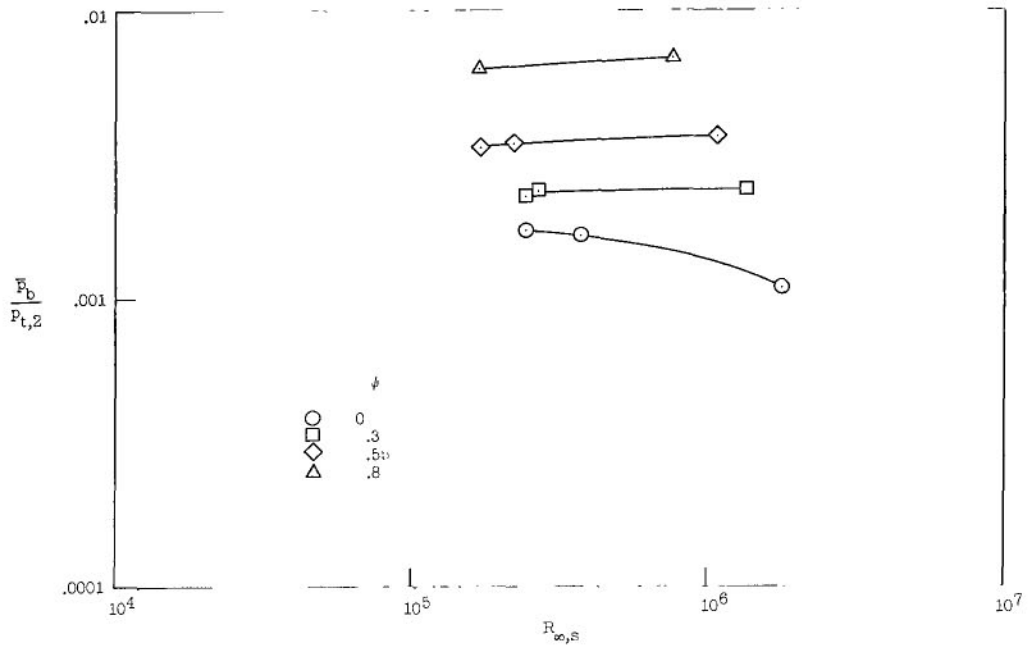

(a) $M_\infty \approx 13.8$.

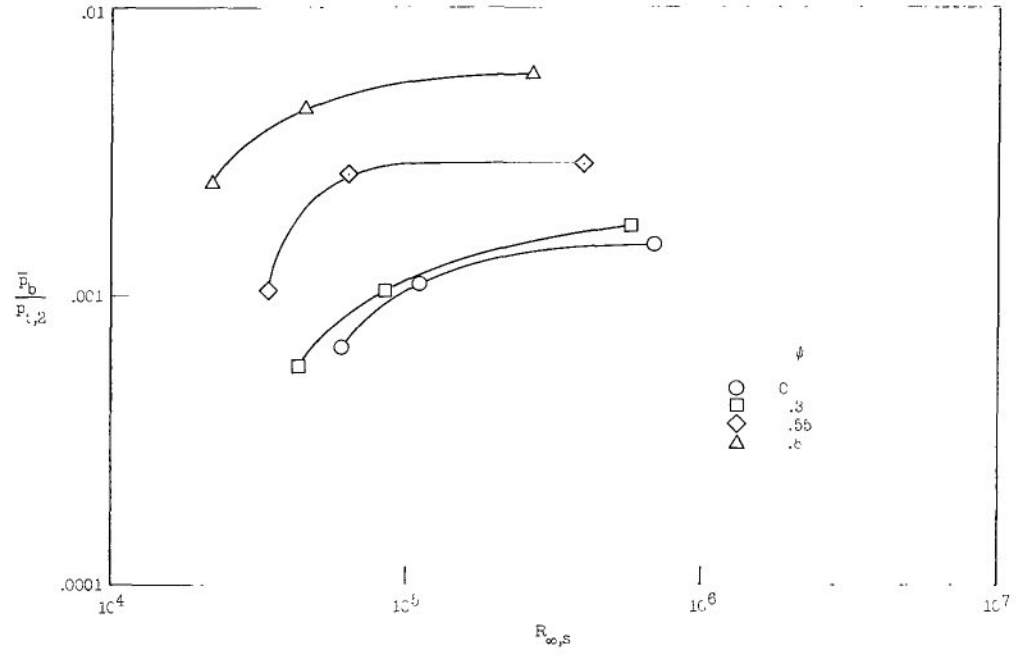

(b) $M_\infty \approx 19.6$.

Figure 9.- Effect of Reynolds number on area-mean base pressure ratio for various bluntness ratios and constant Mach numbers.

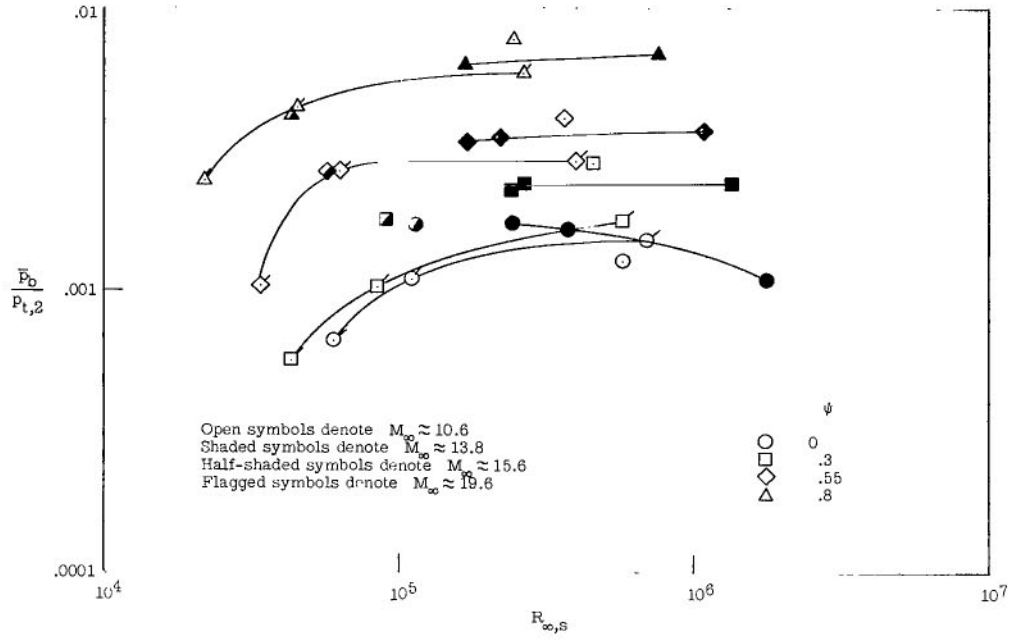

(a) Nondimensionalized by stagnation pressure behind normal shock.

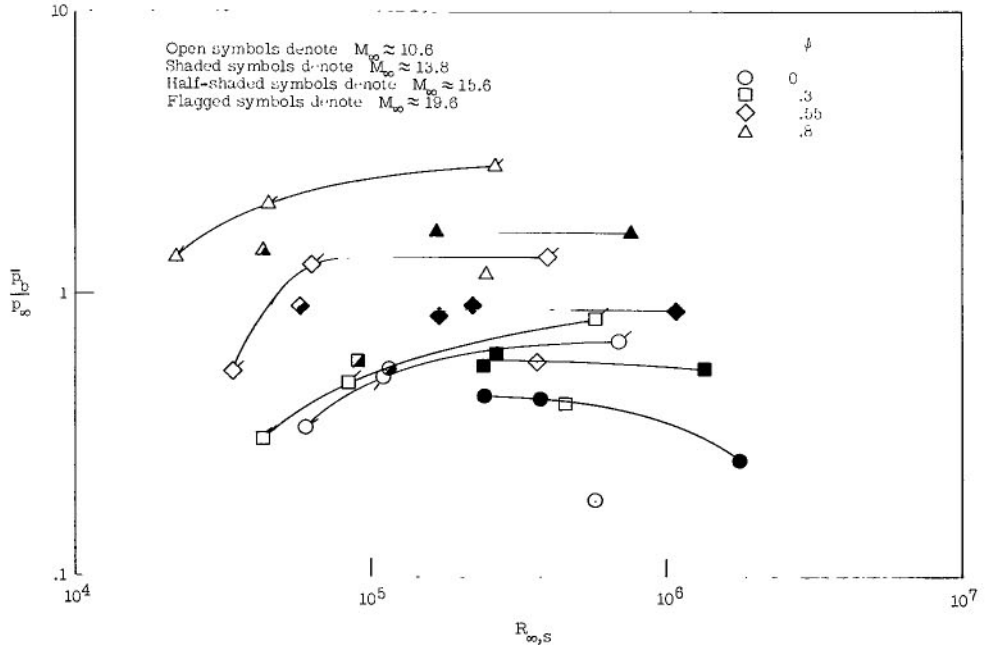

(b) Nondimensionalized by free-stream static pressure.

Figure 10.- Area-mean base pressure ratio as function of Reynolds number for various bluntness ratios and Mach numbers.

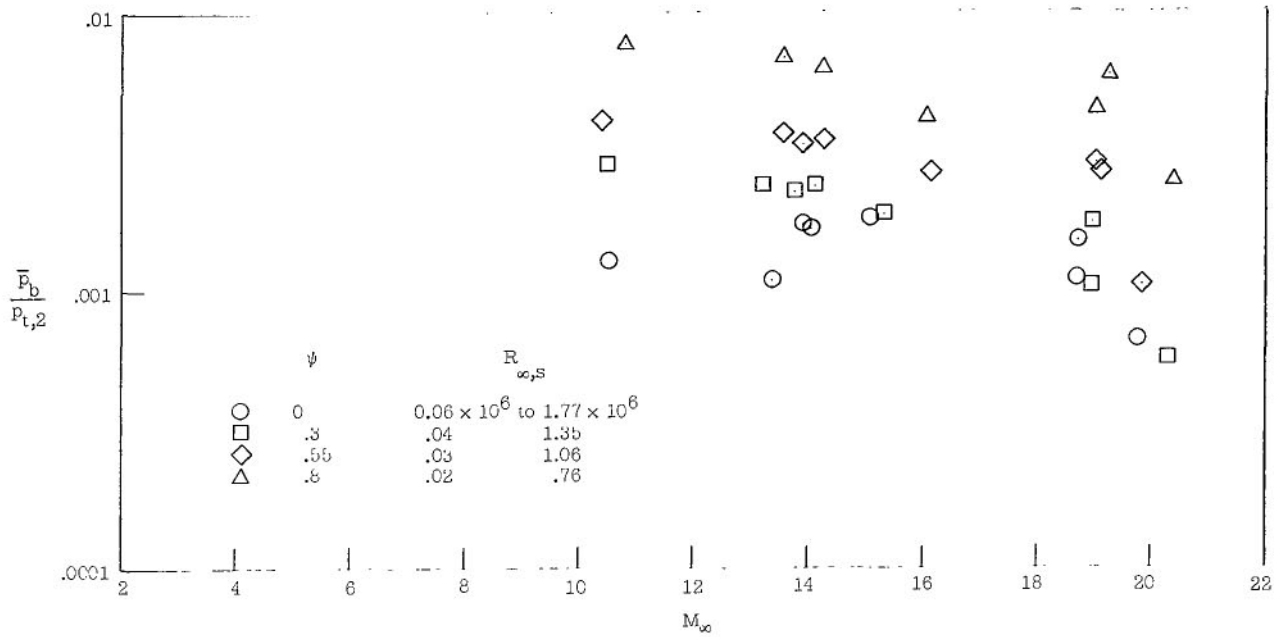

(a) Nondimensionalized by stagnation pressure behind normal shock.

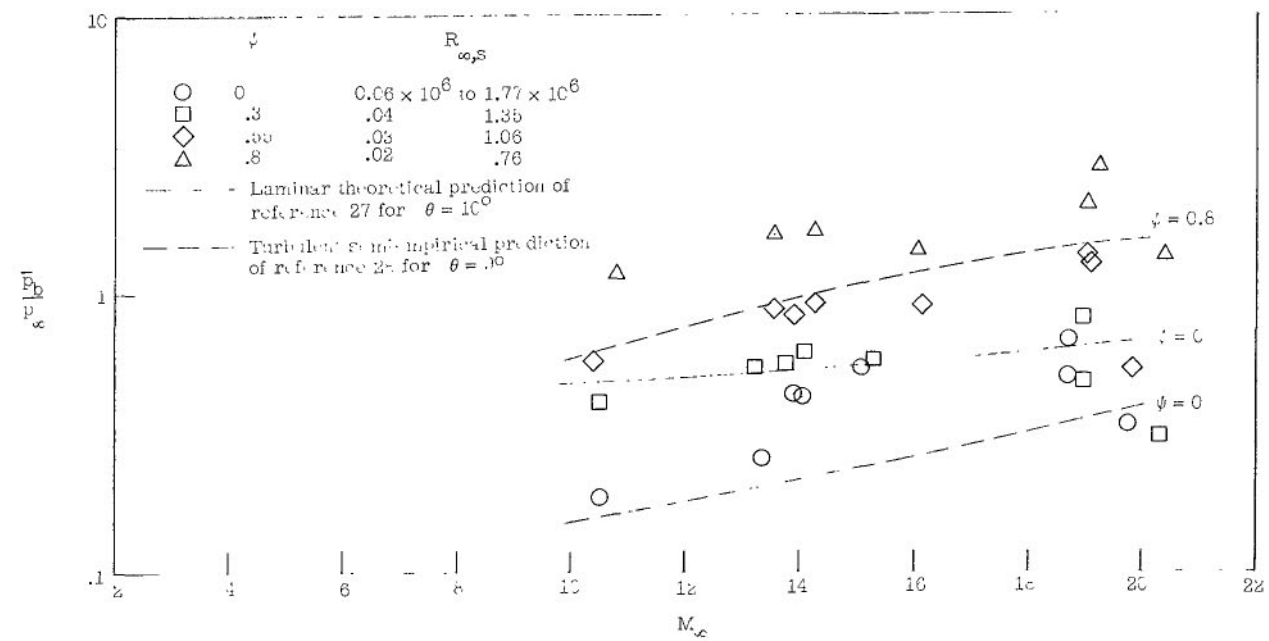

(b) Nondimensionalized by free-stream static pressure.

Figure 11.- Area-mean base pressure ratio as function of Mach number for various bluntness ratios and Reynolds numbers.

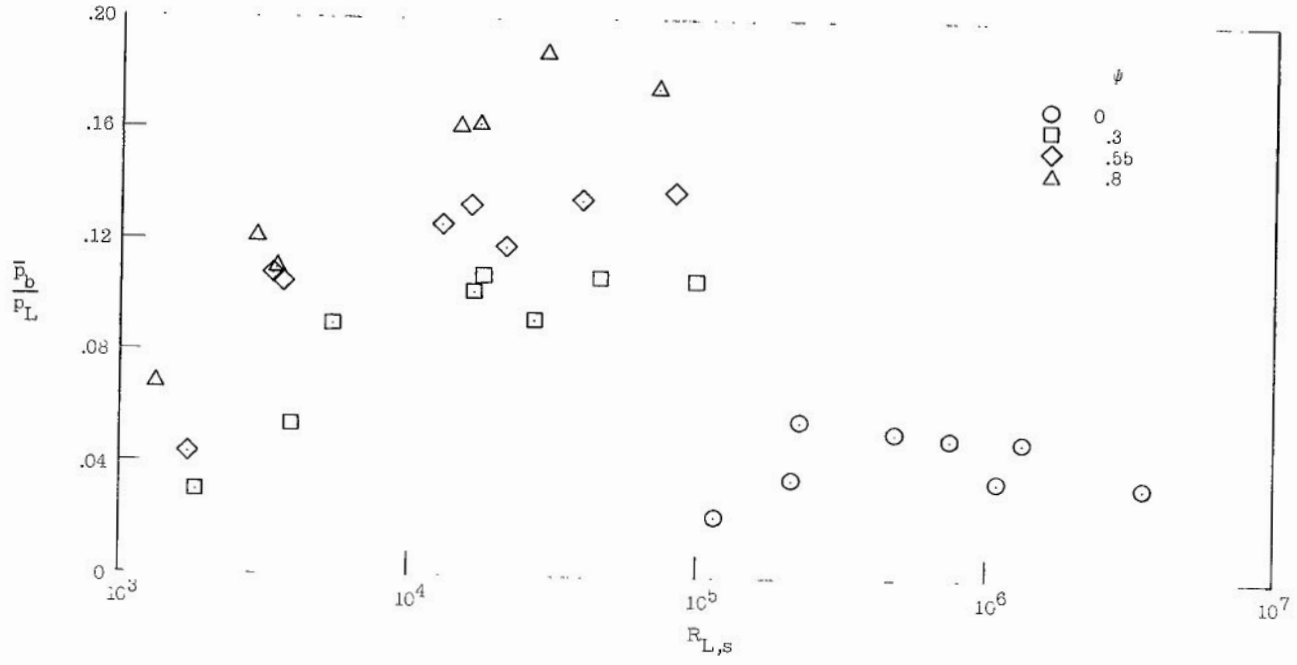

(a) Local Reynolds number.

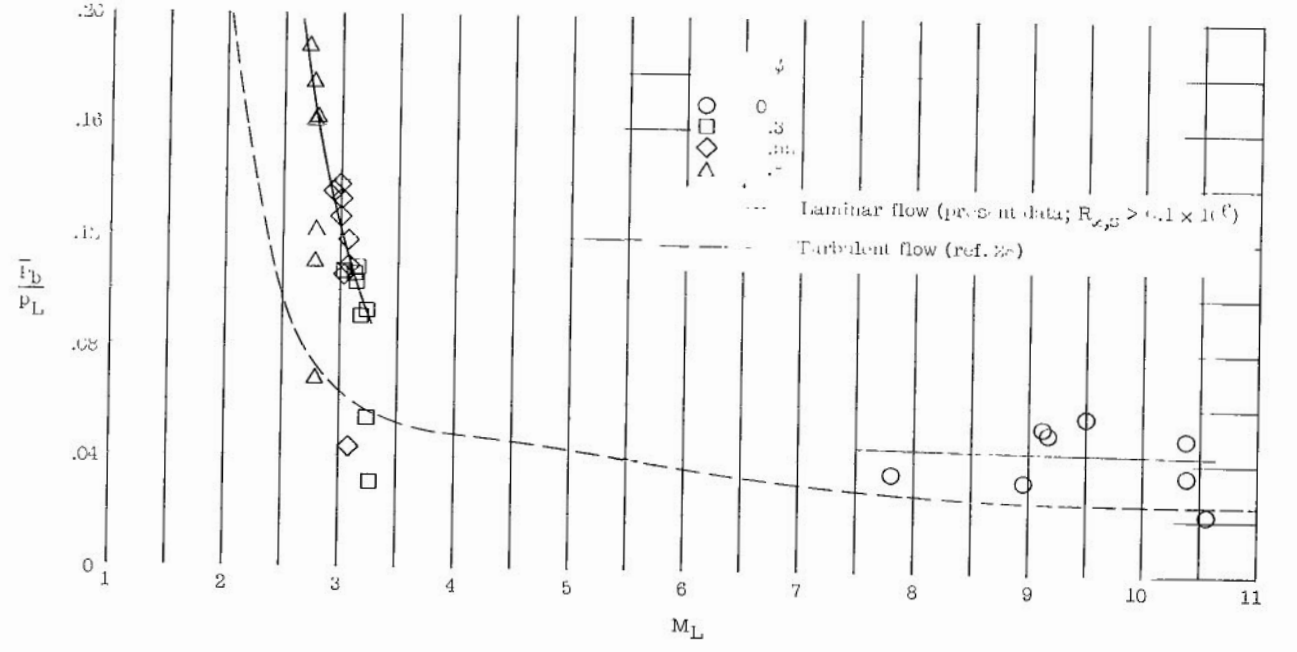

(b) Local Mach number.

Figure 12.- Base pressure in terms of local conditions immediately ahead of model base as obtained from inviscid flow-field solution.

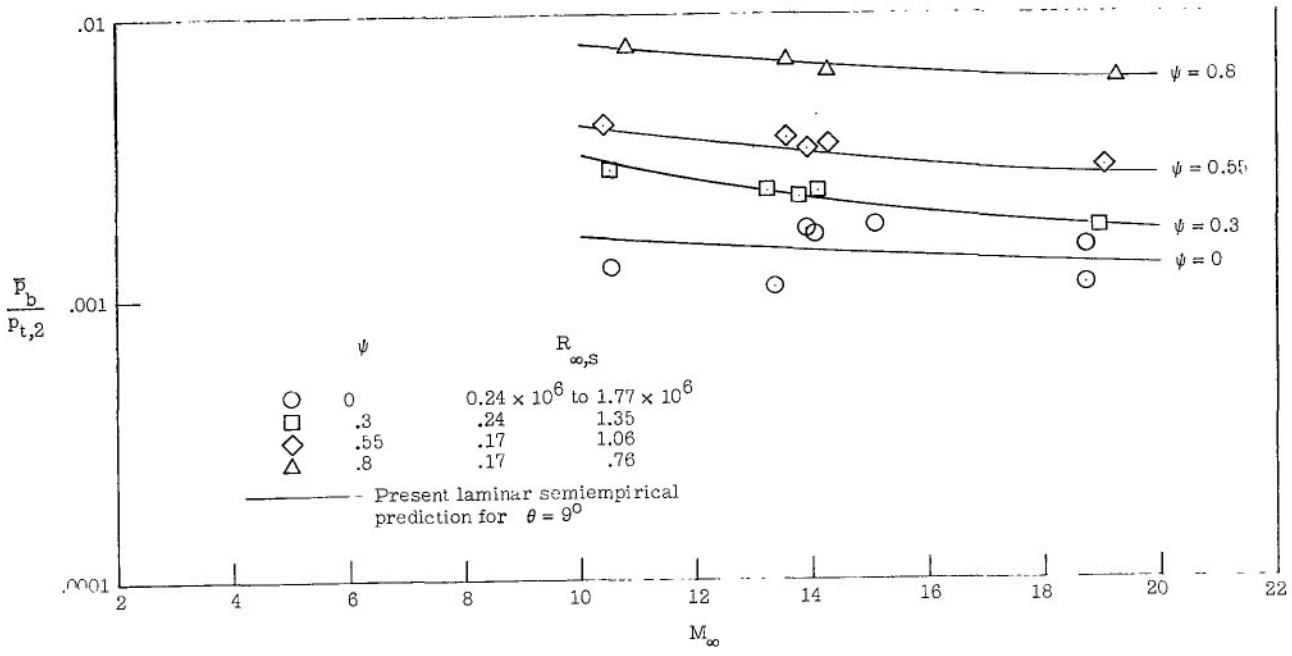

(a) Nondimensionalized by stagnation pressure behind normal shock.

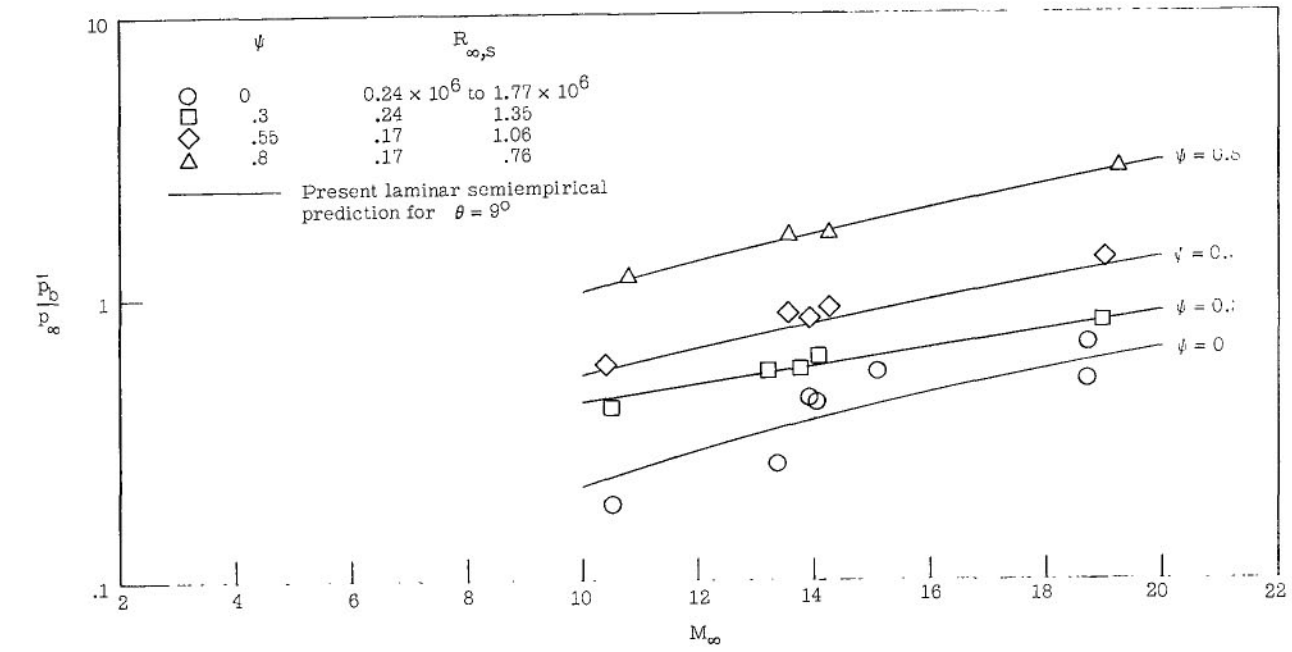

(b) Nondimensionalized by free-stream static pressure.

Figure 13.- Prediction of laminar area-mean base pressure ratio for cones having $\theta = 90^o$. $M_\infty > 10$; $0.1 \times 10^6 \leq R_{\infty,s} \leq 1 \times 10^6$.

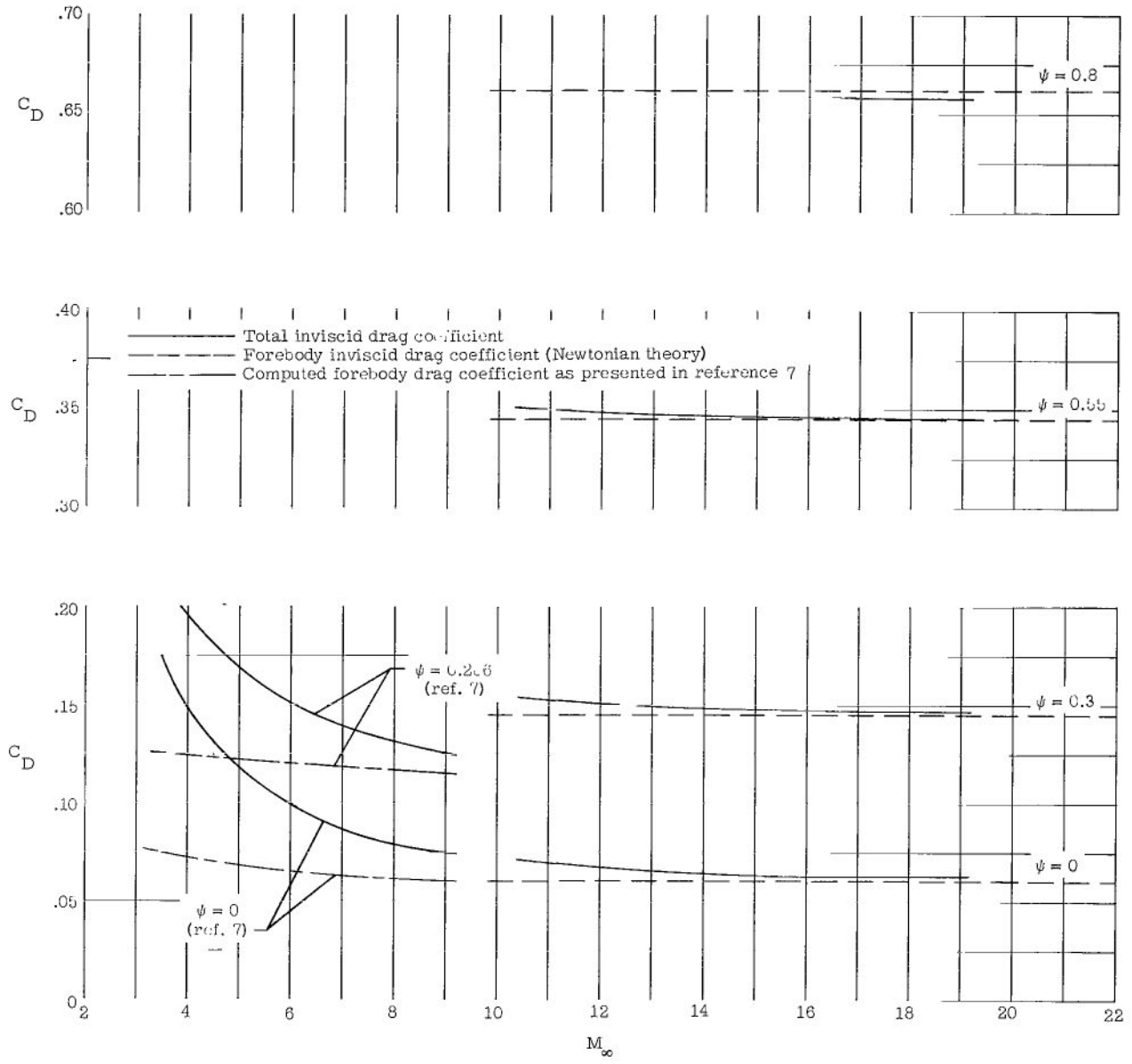

Figure 14.- Base drag contribution for 9^0 cones having various bluntness ratios.

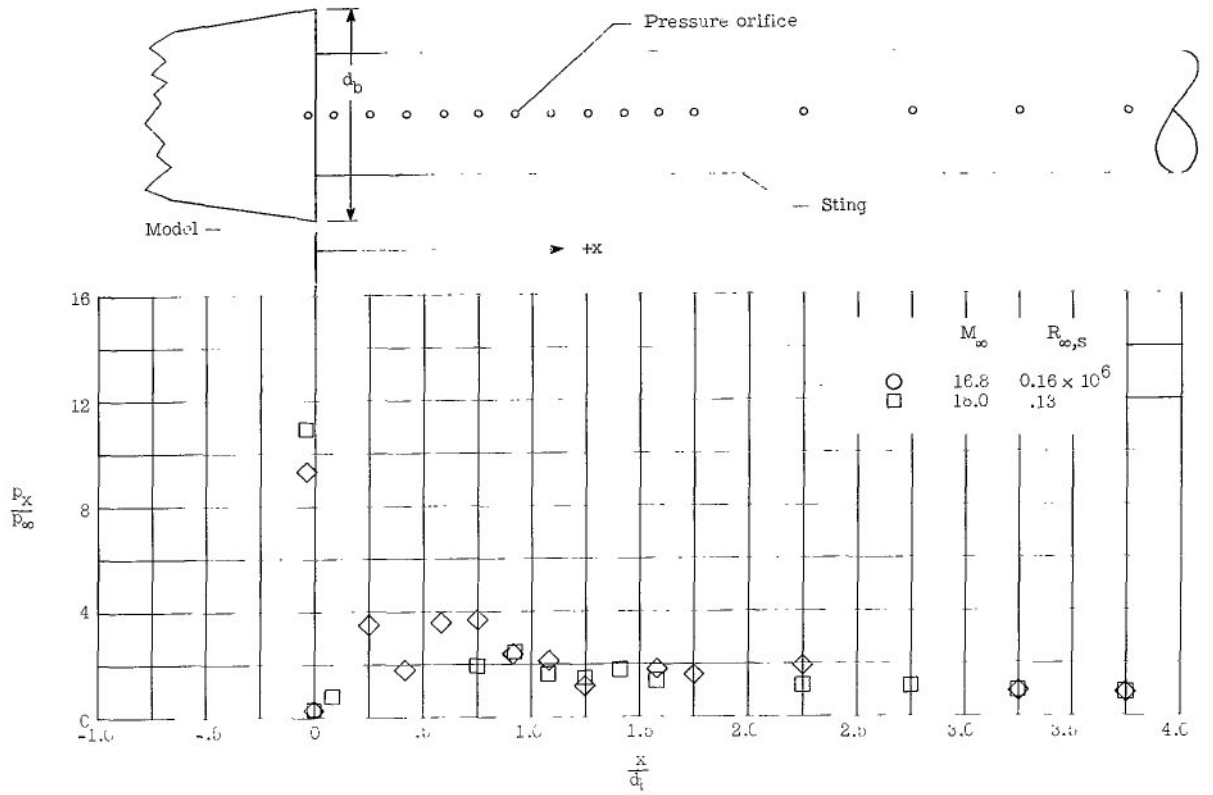

(a) $\psi = 0$.

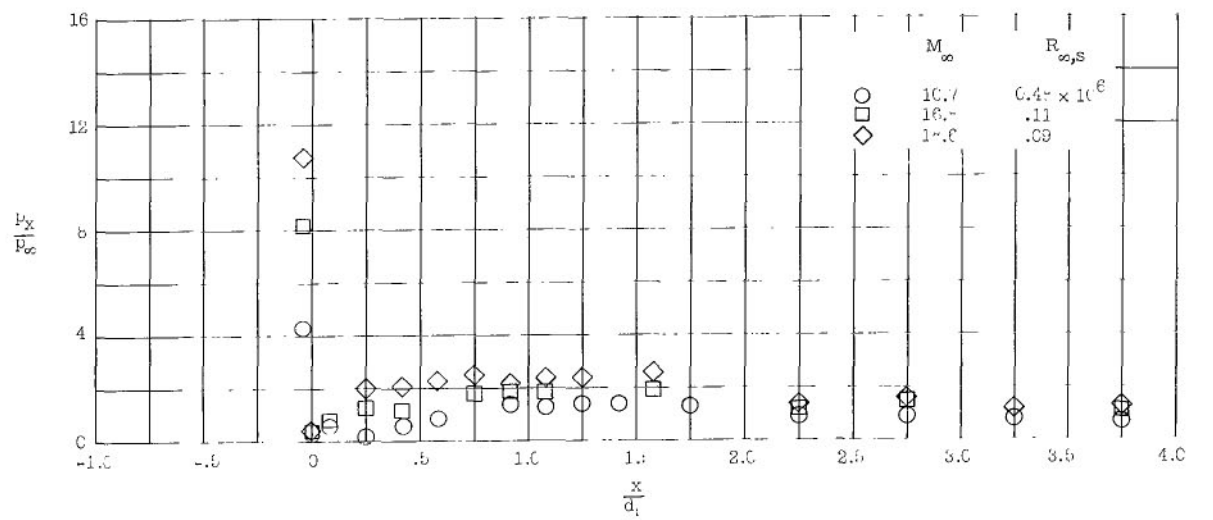

(b) $\psi = 0.3$.

Figure 15.- Sting surface pressure distributions for various bluntness ratios. $l/d_b = 12$; $D/d_b = 0.583$; $r_y/r_b = 0.833$.

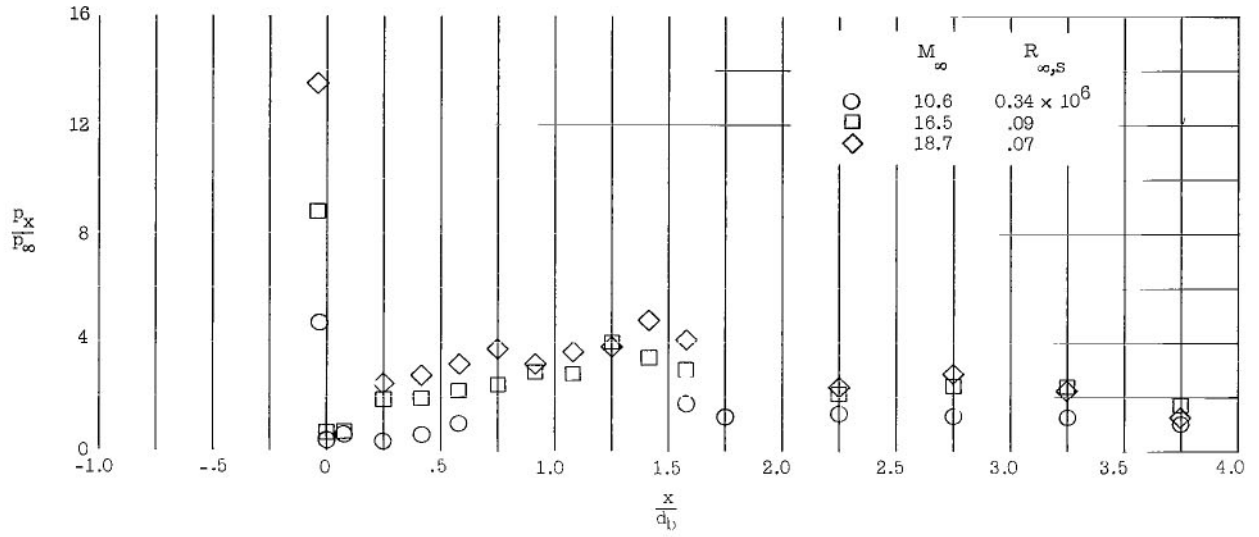

(c) $\psi = 0.55$.

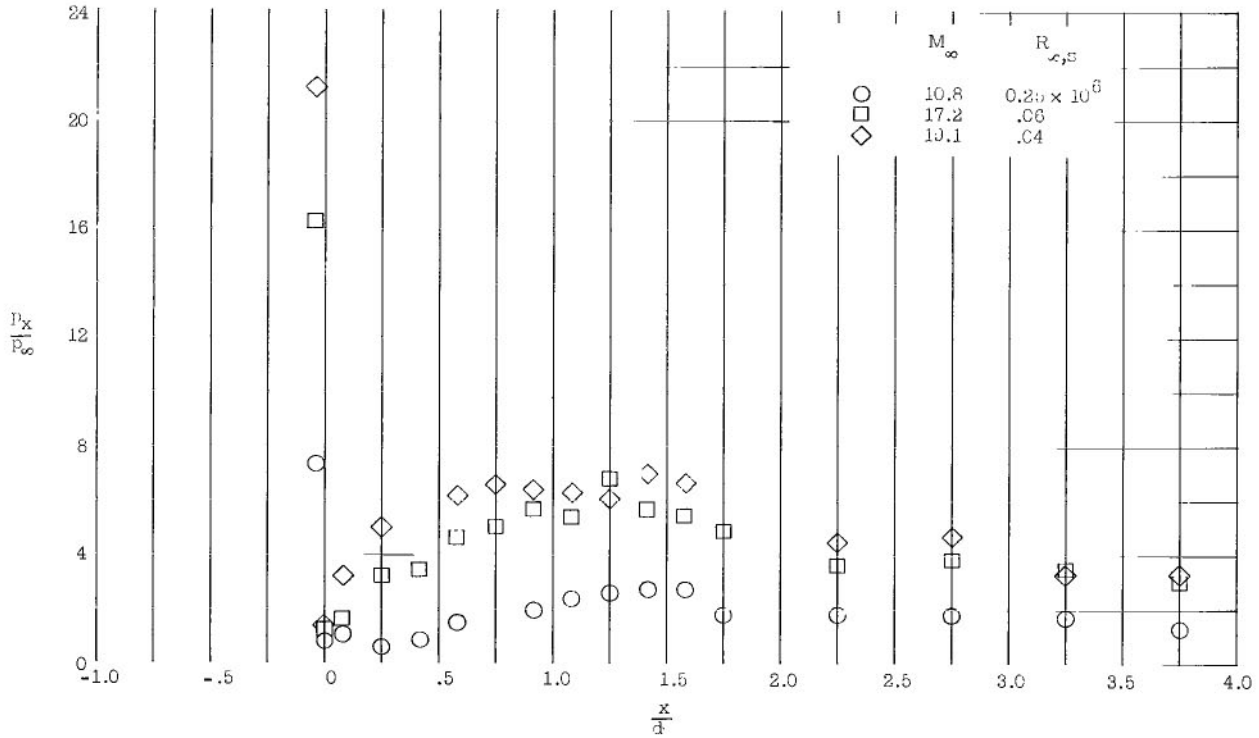

(d) $\psi = 0.8$.

Figure 15.- Concluded.

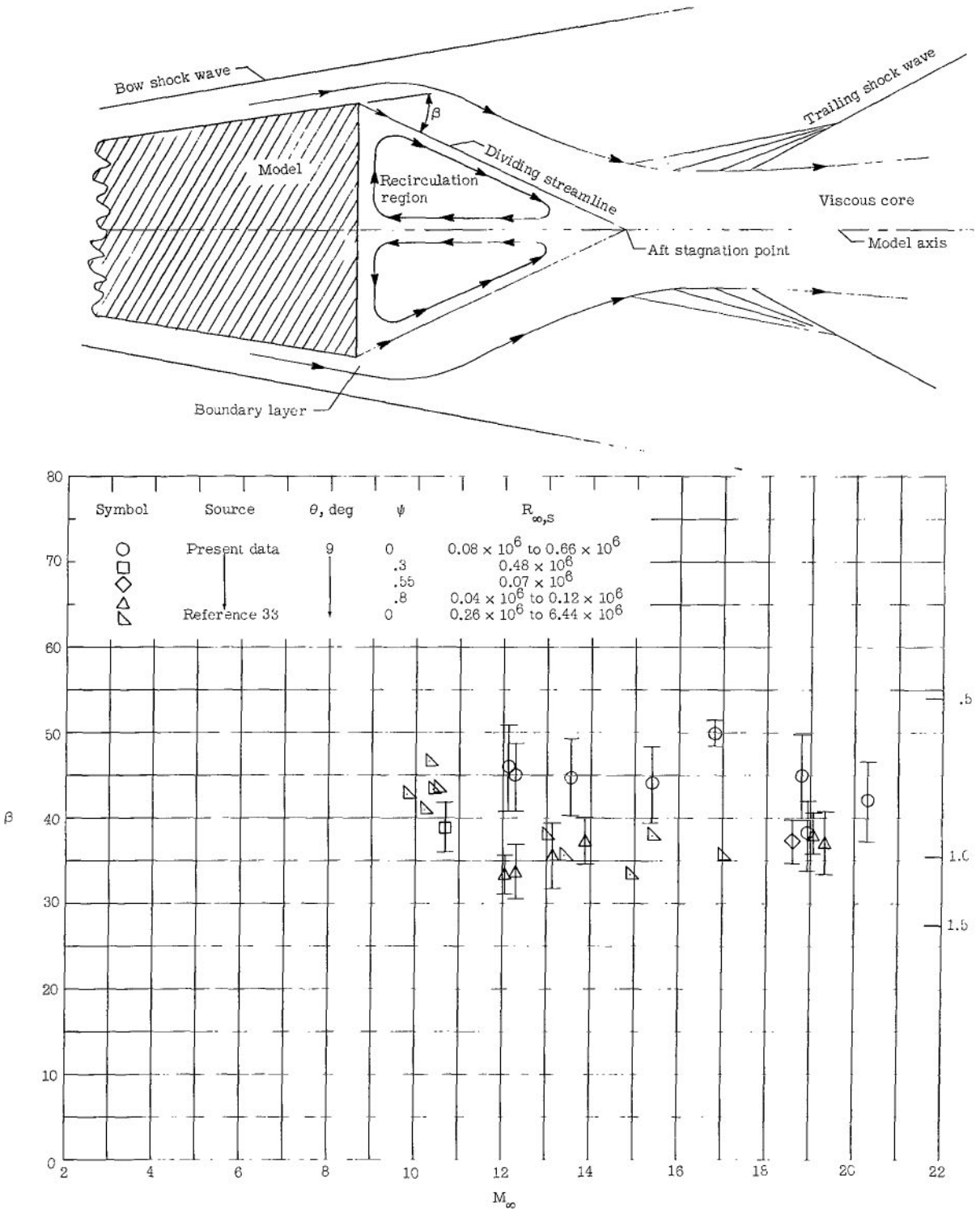

Figure 16.- Dividing-streamline turning angle as function of Mach number. $l/d_b = 12$; $D/d_b = 0.583$.

"The aeronautical and space activities of the United States shall be conducted so as to contribute . . . to the expansion of human knowledge of phenomena in the atmosphere and space. The Administration shall provide for the widest practicable and appropriate dissemination of information concerning its activities and the results thereof."

—NATIONAL AERONAUTICS AND SPACE ACT OF 1958

NASA SCIENTIFIC AND TECHNICAL PUBLICATIONS

TECHNICAL REPORTS: Scientific and technical information considered important, complete, and a lasting contribution to existing knowledge.

TECHNICAL NOTES: Information less broad in scope but nevertheless of importance as a contribution to existing knowledge.

TECHNICAL MEMORANDUMS: Information receiving limited distribution because of preliminary data, security classification, or other reasons.

CONTRACTOR REPORTS: Scientific and technical information generated under a NASA contract or grant and considered an important contribution to existing knowledge.

TECHNICAL TRANSLATIONS: Information published in a foreign language considered to merit NASA distribution in English.

SPECIAL PUBLICATIONS: Information derived from or of value to NASA activities. Publications include conference proceedings, monographs, data compilations, handbooks, sourcebooks, and special bibliographies.

TECHNOLOGY UTILIZATION PUBLICATIONS: Information on technology used by NASA that may be of particular interest in commercial and other non-aerospace applications. Publications include Tech Briefs, Technology Utilization Reports and Notes, and Technology Surveys.

Details on the availability of these publications may be obtained from:

SCIENTIFIC AND TECHNICAL INFORMATION DIVISION

NATIONAL AERONAUTICS AND SPACE ADMINISTRATION

Washington, D.C. 20546